# Hyperfine Structure of the Metastable State of Singly Ionized Helium-3*

ROBERT NOVICK† AND EUGENE D. COMMINS‡§
*Columbia Radiation Laboratory, Columbia University, New York, New York*
(Received March 18, 1958)

The hfs splitting $\Delta\nu$ of the metastable state of singly ionized helium 3 is determined by an ion-beam method. The conventional inhomogeneous molecular-beams $A$ and $B$ fields are replaced by radio-frequency fields at 13 350 Mc/sec. At this frequency transitions are preferentially induced between the $F=1$ component of the $2\,^2S_{\frac{1}{2}}$ state and the short-lived $2\,^2P_{\frac{1}{2}}$ state. All those ions which have made the transition decay immediately to the ground state. Thus, as the beam passes through such a field, state-selection is accomplished by selective quenching of the $F=1$ metastable ions. Two types of detection have been used: photoelectric detection of the Lyman-alpha photons emitted in the second state selector, and metastable ion detection by the surface Auger effect.

Eighty-six determinations of the hfs splitting have been made under a range of experimental conditions. The final result is $\Delta\nu=1083.35499\pm0.00020$ Mc/sec. This value is compared with the theoretical hfs splitting for a point nucleus, which includes the known electrodynamic, relativistic, and reduced-mass corrections, and which may be computed precisely, since the atomic wave function of $He^{3+}$ is hydrogenic and known exactly. The observed hfs splitting is smaller by 186 ppm than the theoretical value. This anomaly is attributed to the effects of finite nuclear and nucleon size, higher order radiative effects, and possibly also to nuclear interaction currents. Estimates are made of some of these effects.

The hfs splitting $\Delta\nu(1s)$ of the ground state of $He^{3+}$ is estimated on the basis of the present result to be $\Delta\nu(1s)=8665.628\pm0.013$ Mc/sec.

The experimental result is also compared with the experimentally determined hfs splitting of the $1s2s$ $(^3S_1)$ state of the $He^3$ atom. The ratio of these two quantities yields a precise estimate of the electronic charge density at the nucleus of the $2\,^3S_1$ state of the $He^3$ atom.

Finally, the monoenergetic nature of the ion beam has allowed observation of a new molecular beams resonance power sharpening effect.

## I. INTRODUCTION

In recent years a number of authors have discussed the theory of the three-body nuclei, helium-3, and tritium. In particular, Sessler and Foley[1] have shown that a contribution to the $S$-state hfs splittings of $He^3$ and $He^{3+}$ of the order of one part in $10^4$ is to be expected from the effects of nuclear structure and possibly also from the effects of nuclear interaction currents. Unfortunately, knowledge of the $He^3$ nuclear wave function and interaction-current Hamiltonian is at present so imperfect that it is impossible to estimate these effects with precision.[2] On the other hand, the absence of any observable hfs anomaly in tritium[3] implies that the interaction current effects in the $H^3$ nucleus are small.[4] If this is also the case for $He^3$, an experimental determination of the hfs will provide a test of proposed $He^3$ nuclear wave functions. Alternatively such an experimental determination, taken together with independent information about the nuclear wave function, may give insight into the precise nature of the $He^3$ nuclear interaction currents.

The hfs splitting of the $2\,^3S_1$ state of the $He^3$ atom, $\Delta\nu(He^3, 2\,^2S_1)$, has been determined by Weinreich and Hughes,[5] but their results cannot be used to study the effects discussed above, because of uncertainties in existing two-electron wave functions.[6] On the other hand, the electronic wave function of $He^{3+}$ is hydrogenic and known exactly. Thus deviations of the observed hfs splitting of the ion from that calculated for a point-dipole nucleus may be interpreted in terms of the above-mentioned nuclear effects.

In the present paper we describe an experimental determination of the hfs splitting of the metastable state of $He^{3+}$, $\Delta\nu(He^{3+}, 2\,S_{\frac{1}{2}})$, by an ion-beam method. The metastable state was chosen for study simply because a method of observation appeared feasible, whereas no practical method has been proposed for the ground state. Unfortunately, an inherent difficulty is associated with the metastable state; namely there exists the possibility of a Stark shift in the hfs splitting due to electric field mixing of the $2\,^2S_{\frac{1}{2}}$ state with close-lying $2P$ states. The experimental apparatus has thus been designed to minimize spurious electric fields along the beam trajectory.

A preliminary value of $\Delta\nu(He^{3+}, 2\,^2S_{\frac{1}{2}})$, hereafter denoted by $\Delta\nu$, was reported in a previous publication.[7] Since that time a number of important changes have been made in the apparatus. The quality of the rf used to induce hyperfine transitions has been improved, the method of detection has been changed, and the apparatus has been generally stabilized. In addition, a systematic search has been made for shifts in the resonance line under observation. It was thus discovered that the preliminary value of $\Delta\nu$ was in error because of

* Work supported in part by the National Science Foundation and jointly by the Signal Corps, the Office of Naval Research, and the Air Force Office of Scientific Research.

† Present address: Department of Physics, University of Illinois, Urbana, Illinois.

‡ Submitted in partial fulfillment of the requirements for the degree of Doctor of Philosophy in the Faculty of Pure Science, Columbia University.

§ Union Carbide and Carbon predoctoral fellow, 1955–1956. RCA predoctoral fellow, 1956–1957.

[1] A. M. Sessler and H. M. Foley, Phys. Rev. **98**, 6 (1955).

[2] M. Verde, *Handbuch der Physik* (Springer-Verlag, Berlin, 1957), Vol. 39, p. 144. A comprehensive discussion of the problem of the three-body nucleus is given.

[3] A. G. Prodell and P. Kusch, Phys. Rev. **106**, 78 (1957).

[4] A. M. Sessler and H. M. Foley, Phys. Rev. **94**, 761 (1954).

[5] G. Weinreich and V. Hughes, Phys. Rev. **95**, 1451 (1954).

[6] W. B. Teutsch and V. Hughes, Phys. Rev. **95**, 1461 (1954).

[7] R. Novick and E. Commins, Phys. Rev. **103**, 1897(L) (1956).

a shift resulting from overlap of $\Delta F=1$, $\Delta m_F=0$ ($\sigma$) and $\Delta F=1$, $\Delta m_F=\pm 1$ ($\pi$) transitions. The overlap condition was eliminated when final observations were made.

On the basis of the splitting observed in the metastable state and the theory of the hfs of hydrogenic systems it is possible to make a precise estimate of the hfs splitting of the ground state of the $He^3$ ion. Furthermore, a comparison of the present experimental result with the experimentally determined hfs splitting of the $1s2s$ ($2\,^3S_1$) state of the $He^3$ atom[5] yields a precise estimate of the electronic charge density at the nucleus of the $2\,^3S_1$ state of the $He^3$ atom. Finally, the monoenergetic character of the ion beam has permitted observation of new details of molecular-beam resonance phenomena. In particular, a resonance power sharpening effect has been observed.[8]

## II. GENERAL METHOD

The method of atomic beams, as it applies to the study of hyperfine structure, most commonly utilizes the deflection of a beam of neutral atoms in an inhomogeneous magnetic field for the purpose of state selection.[9] An alternative scheme was employed for the special case of metastable hydrogen by Heberle, Reich, and Kusch.[10] In their experiments state selection was effected by allowing a beam of metastable atoms to pass through a field of 575 gauss. At this field the $2\,^2S_{\frac{1}{2}}$ ($m_J=-\frac{1}{2}$) and $2\,^2P_{\frac{1}{2}}$ ($m_J=\frac{1}{2}$) levels cross, and the atoms in the former level are selectively quenched by the small motional electric field.

Unfortunately neither method is appropriate for $He^{3+}$. With conventional $A$ and $B$ magnets, and at a practical ion-beam velocity of $10^6$ cm/sec, the Lorentz force would be of the order of $10^6$ times greater than the deflecting force on a magnetic moment of one Bohr magneton. However, if the Lorentz force were to be compensated for by, for example, crossed electric and magnetic fields, it would be necessary to select a prohibitively narrow band of beam velocities, since compensation would be complete only at one velocity. Thus the conventional deflection method appears impractical for ion beams. An extension of the Heberle-Reich-Kusch method to $He^{3+}$ seems quite unfeasible as well. The crossing point of the appropriate $2\,^2S_{\frac{1}{2}}$ and $2\,^2P_{\frac{1}{2}}$ levels in $He^{3+}$ occurs at about 7600 gauss, and it would be difficult to prevent fields of this magnitude from fringing into the hfs transition region, where it is required that the static magnetic field be small and uniform. Moreover, the ion optics would be considerably complicated by the presence of such large fields as are required for the level crossing in this case.

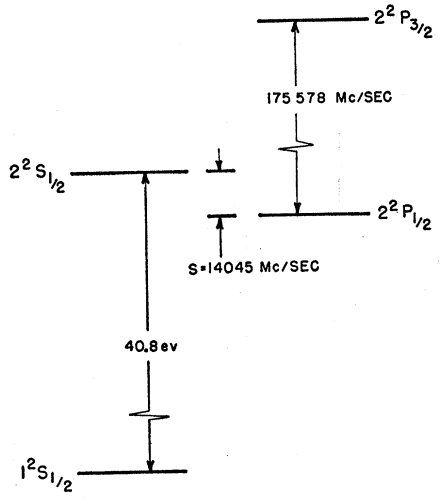


FIG. 1. Main features of the energy level structure of $He^{3+}$ for the $n=1$ and $n=2$ states. Hfs is neglected.

In the present experiment state selection is achieved instead by means of radio-frequency transitions. In order to describe the effect of these transitions in detail, we review the level structure of $He^{3+}$ briefly.

Separated from the $1\,^2S_{\frac{1}{2}}$ ground state of $He^{3+}$ by approximately 40.8 ev are the $2S$ and $2P$ states (see Fig. 1). The $2\,^2S_{\frac{1}{2}}$ and $2\,^2P_{\frac{1}{2}}$ states are themselves separated by a Lamb shift of approximately 14 045 Mc/sec.[11] An ion in the $2\,^2P_{\frac{1}{2}}$ state, which lies lower in energy, may make a direct electric-dipole transition to the ground state with the emission of a 303.8 A Lyman-alpha photon. The mean life of the $2\,^2P_{\frac{1}{2}}$ state is only $10^{-10}$ second, and its corresponding half-width is 1600 Mc/sec. On the other hand, an ion in the $2\,^2S_{\frac{1}{2}}$ state may make no direct electric-dipole transition to the ground state, its most likely mode of decay being by double-quantum emission.[12] This state is therefore metastable, with an estimated mean lifetime of approximately two milliseconds in the absence of perturbing fields. Both states exhibit hyperfine structure, inverted because the nuclear magnetic moment of $He^3$ is negative.[13] Figure 2 illustrates the Zeeman effect of the hyperfine structure.[14]

In the present experiment $He^3$ atoms are ionized by electron bombardment in an electrostatically focused ion source (see Fig. 3). Approximately 1% of the ions formed is metastable. The ions are drawn out of the bombardment region and accelerated to form a beam, which is then focused by an electrostatic lens. The beam energy has been, at various times, 5, 10, 20, or 40 ev. Initially the four sublevels of the metastable state are approximately equally populated. After

[8] E. Commins and R. Novick, Bull. Am. Phys. Soc. Ser. II, **2**, 344 (1957).
[9] N. F. Ramsey, *Molecular Beams* (Oxford University Press, London, 1956).
[10] Heberle, Reich, and Kusch, Phys. Rev. **101**, 612 (1956). The application of the method of rf state selection to the case of $He^3$ was first made by J. Heberle.
[11] The value of $S$ for $He^{3+}$ is obtained from the observed value of $S$ for $He^{4+}$ by applying suitable mass and finite-size corrections. See E. Lipworth and R. Novick, Phys. Rev. **108**, 1434 (1957).
[12] G. Breit and E. Teller, Astrophys. J. **91**, 215 (1940).
[13] M. Klein and B. Holder, Phys. Rev. **106**, 837(L) (1957).
[14] G. Breit and I. I. Rabi, Phys. Rev. **38**, 2082 (1931).

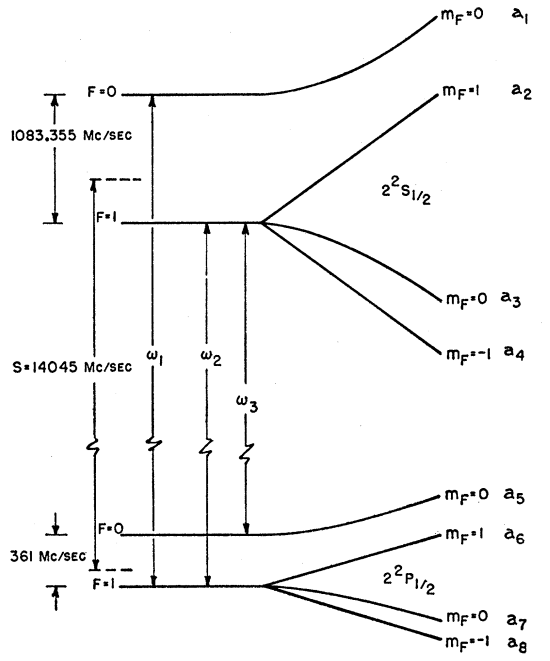


FIG. 2. Zeeman effect in the hfs of the $2\,^2S_{\frac{1}{2}}$ and $2\,^2P_{\frac{1}{2}}$ states of $He^{3+}$.

passing through the first lens the beam enters a wave guide driven at 13 350 Mc/sec. At this frequency transitions are preferentially induced from the $F=1$ level of the metastable state to one of the $2\,^2P_{\frac{1}{2}}$ substates. Those ions which have made the transition decay to the ground state in the mean time of $10^{-10}$ second, producing a net population difference between the hfs levels. Since the natural width of the $2\,^2P_{\frac{1}{2}}$ state is of the order of magnitude of the hfs splitting of the metastable state, it is impossible to avoid depopulating the $F=0$ metastable state to some extent, but for a proper choice of rf power and frequency, the $F=1$ state is depopulated much faster. Thus, as the ion beam leaves the first state selector or "polarizer" there are about three times as many metastables in the $F=0$ state as in each of the three $F=1$ substates.

The beam then traverses the hfs transition region, over whose entire length exists a weak static magnetic field. Since the ion beam is virtually monoenergetic, nearly all the $F=0$ metastables make the transition

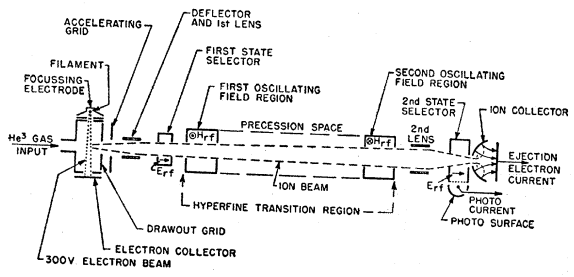


FIG. 3. Schematic diagram of the experimental apparatus.

to the $F=1$ state for a proper choice of rf power, frequency, and polarization. The angle between static and rf magnetic fields may be controlled by means of compensating coils external to the vacuum chamber, so that the relative intensities of the $\sigma$ and $\pi$ transitions may be chosen at will. Two types of transition region have been used, the separated oscillating field type due to Ramsey[15] and a simple uniform field type. The latter was introduced in the later stages of the experiment to reduce the overlap effects mentioned above.

After passing through the hfs transition region, the beam traverses a second focusing lens and then a second waveguide, or "analyzer," again driven at 13 350 Mc/sec. Once more transitions are preferentially induced from the $F=1$ level of the metastable state to the $2\,^2P_{\frac{1}{2}}$ state, and again all those ions which have made the transition quickly decay to the ground state with the emission of Lyman-alpha photons.

Two distinct methods have been used to detect the hfs transitions. Both are illustrated schematically in Fig. 3, although only one was used at any given time. First, one may detect photoelectrically the Lyman-alpha radiation emitted during decay of the metastables in the analyzer. When no hfs transitions occur, relatively few of the metastables entering the analyzer are in the $F=1$ state, and the photocurrent is at a minimum. At an optimum rf power and frequency in the hfs transition region, many transitions occur, and a relatively large number of metastables entering the analyzer are in the $F=1$ state; the photocurrent is consequently a maximum. Alternatively, one may observe the number of metastables surviving the analyzer by observing the electrons ejected from the ion collector by the impinging ion beam. Both metastable ions and ground-state ions eject electrons, but the electron yield-per-metastable is much greater. When no hfs transitions occur, a maximum number of metastables survive the analyzer, and the ejection electron current is a maximum; when most hfs transitions occur, the electron current is a minimum. With this detector it is necessary to eliminate the effects of the large background of electrons ejected by ground-state ions. This is done by modulating the rf power in the polarizer, and observing only the modulated component of the ejection electron current.

The method described in the foregoing may in principle be applied to the $2S$ state of any hydrogenic atom or ion. However, aside from the difficulty of producing multiply charged metastable ions, there is the further difficulty that the polarization and analysis frequency increases roughly as the fourth power of the nuclear charge $Z$. For all but the very lightest nuclei, this frequency is beyond the range of present day microwave generators. Moreover, with increasing $Z$ the width of the $2P$ state increases more rapidly than the hfs splitting. This has the effect of reducing the

[15] N. F. Ramsey, Phys. Rev. **78**, 695 (1950).

efficiency of state selection and thus diminishing the useful signal. In the case of the doubly charged lithium isotopes, the polarizing frequency is about 60 000 Mc/sec, the width of the $2P$ state is 8060 Mc/sec, and the hfs separations are about 1060 Mc/sec and 3740 Mc/sec for the lighter and heavier isotopes, respectively. For heavier ions the situation is even worse, and it appears that the present method is limited to $He^{3+}$, $H^3$, and $H^1$. The small hfs splitting of deuterium precludes the use of an rf method of state selection in that case.[16]

### III. PRODUCTION OF METASTABLE IONS

The cross section for the production of ground-state helium ions by electron bombardment, denoted by $\sigma^+(1S)$, has been determined experimentally,[17] but no similar information is available for $\sigma^+(2S)$, the cross section for production of metastable ions. On the basis of the sudden approximation, a simple estimate gives[18]

$$\sigma^+(2S)=0.01\sigma^+(1S)=3.3\times10^{-19}\ \text{cm}^2. \quad (1)$$

This estimate is reliable only to an order of magnitude,

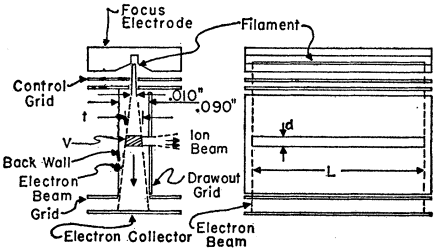


FIG. 4. Schematic diagram of the ion source.

but is sufficiently good for the purpose of designing an ion source. Ionization might be achieved by means of a gas discharge or by bombardment of $He^3$ gas with an electron beam. The latter of these two alternatives was chosen, since several workers had already been successful in producing metastables in this manner.[11,18]

For reasons to be discussed, it is desirable that the ion beam be wide and flat; therefore the bombarding electron beam is shaped as shown in Fig. 4. Electrostatic focusing of the electron beam is employed, since the use of magnetic fields would seriously disturb the trajectory of the slow ion beam and even prevent ions from leaving the source. It may be shown that recoil effects during the ionization process are quite small, so that the ions formed have approximately thermal energies. Quenching of the metastable ions might arise from the effects of space-charge fields, plasma oscillations, and collisions of metastable ions with electrons and atoms. These processes are difficult to analyze in

[16] Reich, Heberle, and Kusch, Phys. Rev. **104**, 1585 (1956).
[17] W. Bleakney, Phys. Rev. **36**, 1293 (1930).
[18] W. E. Lamb, Jr., and M. Skinner, Phys. Rev. **78**, 539 (1950).

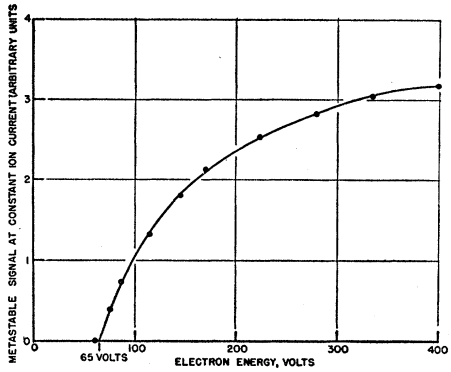


FIG. 5. Excitation curve for the production of metastable ions at constant ion current, plotted as a function of electron bombardment energy.

detail, but observation shows that approximately 1% of the ions in the beam is metastable. This is consistent with the estimate of cross section [Eq. (1)] and suggests that little quenching occurs in the source.

Preliminary observations of the ion source yield were made by placing an accelerator grid and ion collector directly in front of the exit aperture of the source. It was found that over a wide range the ion current, $I_i$, for the short beam was proportional to the electron collector current, $I_c$, and for $I_c=5$ ma and a source pressure of $p=10^{-4}$ mm Hg, the ion current was $I_i=2.5\times10^{-7}$ ampere. This yield was more than adequate since space-charge spreading limited the ion current traversing the full length of the apparatus to about $4.5\times10^{-8}$ ampere at 20-ev beam energy.

It has been possible to determine experimentally the form of $\sigma^+(2S)$, although its scale is not known with precision. Figure 5 illustrates an excitation curve for the production of metastable ions at constant ion current. This curve gives the form of $\sigma^+(2S)/\sigma^+(1S)$, but since $\sigma^+(1S)$ is known,[17] one may determine $\sigma^+(2S)$ as a function of electron energy to a multiplicative constant. The latter cross section is plotted in Fig. 6.

Initially some difficulty was encountered with contamination of the ion beam by slow electrons.

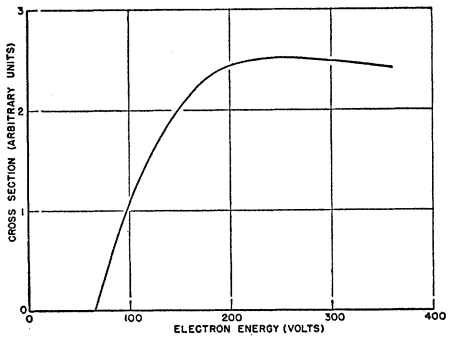


FIG. 6. Cross section for the production of metastable ions, plotted as a function of electron bombardment energy.

TABLE I. Ion-source and beam parameters.[a]

| | |
|---|---|
| Filament length | 2.130 in. |
| Filament diameter | 0.010 in. (tungsten) |
| Filament heating current | 6.0 amperes |
| Filament heating voltage (60 cps) | 6.0 volts (regulated for constant ion current) |
| Cathode voltage | −250 volts |
| Drawout voltage | −2.0 volts |
| Electron collector voltage | +90 volts |
| Focus electrode voltage | −370 volts |
| Electron emission current | 10 ma |
| Electron collector current | 5 ma |
| Ion-beam energy | 20 ev |
| Ion-beam velocity | $3.6\times10^{6}$ cm/sec |
| Ion-beam length | 35 cm |
| Ion-beam cross section (at midpoint of trajectory) | 3 cm×1 cm |
| Ion beam current (maximum, at 20 ev) | $4.5\times10^{-8}$ ampere |
| Ion beam current (typical, at 20 ev) | $2.0\times10^{-8}$ ampere |
| Source pressure (estimated) | $2.5\times10^{-4}$ mm Hg |
| Main chamber pressure (ultimate) | $3\times10^{-8}$ mm Hg[b] |
| Main chamber pressure (during run) | $2\times10^{-5}$ mm Hg[b] |
| Gas flow | 0.1 cc/min STP |

[a] Typical values are given. All voltages are with respect to the source.
[b] Pressure as measured with an ion gauge calibrated for nitrogen.

These proved to be secondaries liberated from the source as the result of collisions of the bombarding electrons with the back wall of the gun (see Fig. 4). The contamination was eliminated by carefully collimating the electron beam and by increasing the width of the bombardment chamber from 0.060 in. to 0.090 in. No appreciable change was observed in electron-beam performance.

Estimates of source performance are contained in Appendix I. A listing of the important ion-source parameters is given in Table I.

## IV. ION OPTICS

The state-selection regions may be either in the form of resonant microwave cavities or nonresonant wave guides excited by pure traveling waves. In the former case the cross-sectional area of the beam is restricted to that portion of the cavity over which the rf electric field has a useful amplitude (about 1 cm²), while in the latter case the area may be made arbitrarily large by extending the beam in the direction of rf propagation. The small beam area associated with cavities restricts the ion current to intolerably low values; on the other hand, the wave guides require large rf power. Fortunately, high-power klystrons were available at the state selection frequency, and the wave guide scheme could be used. Thus the cross section of the beam is large in the direction of propagation of power in the guide and small in the transverse dimension.

None of the usual methods for reducing the effects of space charge and thermal spreading could be employed in the hfs transition region. Magnetic collimation would produce an intolerably large Zeeman effect, while either electrostatic lenses or electron space-charge neutralization might quench the metastable ions and

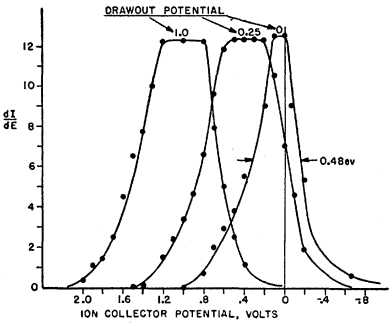


FIG. 7. Differential retarding potential curves showing the distribution of ion energies for three different drawout potentials.

produce a Stark shift in the hfs splitting. The length of the hfs transition region is of the order of 25 centimeters, and for the ion currents employed in the experiment the beam spreads appreciably in this distance. The hfs transition structure must then be made large enough to accommodate the beam, and this in turn necessitates high power.

If an uncertainty of the order of one part per million (1 kc/sec) is to be achieved in the determination of $\Delta\nu$, it is desirable that the linewidth of the observed transition be no greater than 100 kc/sec. This width can be achieved either with a long hfs transition region or with low beam velocities. Since the beam is at least in part space-charge limited in this region, the maximum ion current is given by a Child's law relation. For a space-charge limited beam it can be shown that for a given line width the maximum ion current is proportional to the length of the beam trajectory (see Appendix II). It would then appear that long transition regions are preferable to low beam velocities. However, the rf Stark effect increases linearly with beam velocity for optimum power (see Appendix IV), and for high velocities the possibility of a Stark shift is increased. A compromise must then be made in choice of beam length. In the present apparatus, the total beam trajectory is 35 cm and the length of the transition region is 25 cm. At the midpoint of the beam trajectory, transverse dimensions of the beam are approximately 3 cm by 1 cm. For a beam energy of 20 ev the estimated space-charge limited ion current is $6\times10^{-8}$ ampere, and the line width of the hfs transition is 80 kc/sec. It is estimated that thermal spreading might reduce the ion current by a factor of two (see Appendix III). An ion current of $4.5\times10^{-8}$ ampere has actually been achieved at 20 ev, and it is observed that the maximum ion current varies as the $\frac{3}{2}$ power of the beam voltage. The energy spread of the beam has been observed as a function of drawout potential (see Fig. 7). It can be seen that for a working drawout potential of one volt, the fractional spread is less than ten percent of the beam energy.

In order to maintain stability the ion beam is regulated electronically. A signal voltage derived from the ion collector current drives an amplifier, which in turn controls the electron emission in the ion source.

In this way it has been possible to maintain the ion current constant to within one percent over periods of several hours.

## V. STATE SELECTION

In order to make quantitative estimates of the signal and background to be expected, we must first describe explicitly how each of the sublevels of the metastable state is depopulated by an oscillatory electric field. It will be helpful to refer to Fig. 2. Let us assume that the letters $a_1$, $a_2$, $\cdots$, which label the various sublevels in Fig. 2 also denote the amplitude coefficients of these sublevels. Thus, in general, $a_1=a_1(t)$, etc. If it is assumed that no spurious electric fields occur, the $2\,^2S_{\frac{1}{2}}$ and $2\,^2P_{\frac{1}{2}}$ states are coupled only in the state selectors, where the beam is exposed to oscillatory electric fields close to the Lamb-shift frequency.

The probability amplitudes, $a_1$, $a_2$, etc., are governed by the usual time-dependent equations:

$$i\hbar\dot{a}_m=\sum_n a_n H_{mn}{}' \exp\left[\frac{i(E_m-E_n)t}{\hbar}\right]. \quad m=1,\cdots,8. \tag{2}$$

The oscillating electric field is directed along the beam. If this direction is also chosen as the axis of quantization, the matrix elements of the perturbation are

$$H_{mn}{}'=eE\cos\omega t\langle m|z|n\rangle. \tag{3}$$

Here $E$ is the amplitude of the oscillating field, $\omega$ its circular frequency, and $\langle m|z|n\rangle$ is the matrix element of $z$ between the states $m$ and $n$. Neglecting the antiresonant terms, Eqs. (2) become

$$\begin{aligned}
&\dot{a}_1=-ia_7Ue^{i(\omega_1-\omega)t}, && \dot{a}_5=-ia_3Ue^{i(\omega-\omega_3)t}-\tfrac{1}{2}\gamma a_5,\\
&\dot{a}_2=-ia_6Ue^{i(\omega_2-\omega)t}, && \dot{a}_6=-ia^2Ue^{i(\omega-\omega_2)t}-\tfrac{1}{2}\gamma a_6,\\
&\dot{a}_3=-ia_5Ue^{i(\omega_3-\omega)t}, && \dot{a}_7=-ia_1Ue^{i(\omega-\omega_1)t}-\tfrac{1}{2}\gamma a_7,\\
&\dot{a}_4=+ia_8Ue^{i(\omega_2-\omega)t}, && a_8=+ia_4Ue^{i(\omega-\omega_2)t}-\tfrac{1}{2}\gamma a_8.
\end{aligned} \tag{4}$$

Here, $U=(eE/\hbar)(\sqrt{3}/4)a_0$, where $e$ and $\hbar$ have their usual meanings, $a_0$ is the Bohr radius, and $\gamma$ is the decay constant of the $2P$ state. The quantities $\omega_1$, $\omega_2$, $\omega_3$ are defined in Fig. 2. The terms in $\gamma$ in Eqs. (4) are inserted to account for the spontaneous decay of the $2P$ state. Solving Eqs. (4), we obtain[19]

$$\begin{aligned}
|a_1|^2&=|a_{10}|^2\exp(-\lambda_1 t),\\
|a_2|^2&=|a_{20}|^2\exp(-\lambda_2 t),\\
|a_3|^2&=|a_{30}|^2\exp(-\lambda_3 t),\\
|a_4|^2&=|a_{40}|^2\exp(-\lambda_2 t).
\end{aligned} \tag{5}$$

Here $a_{i0}=a_i(0)$ and $\lambda_i=U^2\gamma/[(\frac{1}{2}\gamma)^2+(\omega_i-\omega)^2]$, $i=1$, 2, 3. Equations (5) show explicitly how the four sublevels are depopulated by the electric field. To describe the composition of the ion beam, let $\phi_1$ be the fractional number of metastables surviving the polarizer, and $\phi_2$ be the fraction of those surviving the polarizer, which also survive the analyzer. Thus, if we denote the fraction of metastables which survive both polarizer and analyzer by $\phi$, we have

$$\phi=\phi_1\phi_2.$$

If we define $I_{1S}$ as the current of ground-state ions and $I_{2S}$ as the current of metastable ions emerging from the analyzer, we have

$$\begin{aligned}
I_{1S}&=I_{1S}{}^0+(1-\phi)I_{2S}{}^0,\\
I_{2S}&=\phi I_{2S}{}^0,
\end{aligned} \tag{6}$$

where $I_{1S}{}^0$ and $I_{2S}{}^0$ are the initial currents of ground-state ions and metastable ions, respectively. The ejection electron current at the surface detector is then

$$I_e=\gamma_{1S}{}^+[I_{1S}{}^0+(1-\phi)I_{2S}{}^0]+\gamma_{2S}{}^+I_{2S}{}^0. \tag{7}$$

Here $\gamma_{1S}{}^+$ and $\gamma_{2S}{}^+$ are the ejection-electron yields for ground-state ions and metastable ions, respectively. The photocurrent in the photoelectric detector is given by

$$I_p=I_{2S}{}^0\phi_1(1-\phi_2)\eta T\Omega/4\pi, \tag{8}$$

where $\mu$ is the fractional photoelectric yield, $T$ is the fractional transmission of the photodetector film and grids, and $\Omega/4\pi$ is the fractional solid angle subtended by the photosurface at the analyzer.

The quantity $\phi$ depends on the rf power and frequency settings in the polarizer and analyzer, as well as in the hfs transition region. There are three separate cases of interest:

1. $\phi'$: Polarizer power off, analyzer power on, no hfs transitions.
2. $\phi''$: Polarizer and analyzer powers on, no hfs transitions
3. $\phi'''$: Polarizer and analyzer powers on, hfs transitions at maximum.

In the case of the surface detector, only the modulated component of the electron current is observed and the useful signal is given by

$$\begin{aligned}
S_S&=[I_e(\phi''')-I_e(\phi')]-[I_e(\phi'')-I_e(\phi')]\\
&=I_e(\phi''')-Ie(\phi''),
\end{aligned} \tag{9}$$

$$S_S=(\gamma_{2S}{}^+-\gamma_{1S}{}^+)(\phi'''-\phi'')I_{2S}{}^0.$$

The background, (the modulation signal with no hfs transitions), is given by

$$B_S=I_e(\phi'')-I_e(\phi')=(\gamma_{2S}{}^+-\gamma_{1S}{}^+)(\phi''-\phi')I_{2S}{}^0. \tag{10}$$

In the photodetector the useful signal is

$$\begin{aligned}
S_p&=I_{2S}{}^0\phi_1(\phi_2''-\phi_2''')T\eta\Omega/4\pi,\\
S_p&=(\phi''-\phi''')I_{2S}{}^0T\eta\Omega/4\pi,
\end{aligned} \tag{11}$$

since $\phi_1$ is independent of the conditions in the hfs transition region. From Eqs. (9) and (11) we see that

[19] In solving Eqs. (4) it is assumed that $U^2\ll\gamma^2$. In the actual experiment $U^2\simeq 10^{-4}\,\gamma^2$.

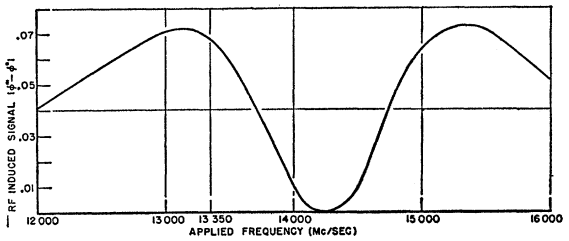


FIG. 8. Rf induced signal for the $\sigma$ transition expressed as a fraction of the total number of metastable ions. The signal is plotted as a function of state-selection frequency, where at each frequency the state selection rf power is adjusted to an optimum value.

the condition on $\phi$ for maximum signal is the same for both detectors; namely that $|\phi'''-\phi''|$ be a maximum. In order to compute $\phi$ explicitly for the various cases of interest, it is convenient to make a table using the results of Eq. (5). In column two of Table II are written the initial population coefficients of the four sublevels of the metastable state; we assume they are equal. Column three gives the values of the population coefficients of these levels after the beam has passed through the polarizer. The beam then passes through the hfs transition region; since the beam is quite monoenergetic, the population coefficients of those substates between which the hfs transitions take place are reversed, for optimum rf power and frequency. Columns four and five indicate this for $\Delta F=+1$, $\Delta m_F=0$ and $\Delta m_F=-1$ transitions, respectively. Since the populations of the $m=0$ and $m=\pm1$ substates of the $F=1$ state are slightly different after the polarizer, it should be possible to observe low-frequency Zeeman transitions. For this case, the coefficients would then be as given in column six. An attempt was made to observe these transitions, but this was unsuccessful, probably because the polarization is very inefficient, and possibly also because Majorana mixing might further reduce the signal. If no transitions occur, the coefficients remain the same as in column three. For the sake of completeness this is given in column seven. After the beam has passed through the analyzer, the metastable population will be further depleted, as indicated in column eight. We may easily compute the quantity $|\phi'''-\phi''|$ for a number of special cases of interest by referring to Table II. As an example, we write $\phi''$, $\phi'''$ for $\Delta m_F=0$, $\Delta F=+1$ transitions. The quantity $\phi''$ is obtained by multiplying the values in column seven by those in column eight and then adding. The quantity $\phi'''$ is obtained as the sum of the products of the values in columns four and eight. Thus,

$$\phi'''-\phi''=-\tfrac{1}{4}(e^{-\lambda_1 t}-e^{-\lambda_3 t})(e^{-\lambda_1' t'}-e^{-\lambda_3' t'}). \quad (12)$$

For optimum signal the polarizer and analyzer transition probabilities are equal and (12) becomes

$$|\phi'''-\phi''|=\tfrac{1}{4}(e^{-\lambda_1 t}-e^{-\lambda_3 t})^2. \quad (13)$$

This quantity is plotted in Fig. 8 as a function of applied frequency, where at each frequency the power is adjusted for optimum signal. The maximum occurs at 13 146 Mc/sec, but it is quite broad. For technical reasons it was decided to operate at 13 350 Mc/sec, which is close to optimum. In this case it may be seen that $|\phi'''-\phi''|=0.069$. Thus only 6.9% of the metastable ions contribute to the useful signal. We summarize some of the principal results of this section in Table III. It should be noted that since the polarizer and analyzer rf power settings have distinct optimum values for the different transitions, the background values in Table III are different. Figure 9 shows the variation of signal for the $\Delta F=1$, $\Delta m_F=0$ transition as a function of the power in one state selector, when the other is at optimum power, and both are driven at 13 350 Mc/sec.

The preceding estimates of $|\phi'''-\phi''|$ are inadequate in that they do not take into account the possibility of mixing of the populations of the three $F=1$ substates (Majorana transitions) between the state selectors. Such mixing may occur if the state selector rf field is not parallel to the static magnetic field. However, the quantities in Table III are reasonably consistent with observed beam intensities and signals. This will be considered in more detail in Sec. VIII.

The state selectors themselves are sections of wave guide appropriately modified with gridded apertures to allow passage of the ion beam. Each state selector is driven at 13 350 Mc/sec by a Varian V-28 klystron, and the rf power is brought into the vacuum chamber through mica windows of 0.004 in. thickness. Either

TABLE II. Metastable population coefficients.[a]

| State | Initial population | Population after polarizer | Population after hfs transition region for the transitions indicated below: $\Delta m_F=0$, $\Delta F=1$ | $\Delta m_F=-1$, $\Delta F=1$ | $\Delta m_F=-1$, $\Delta F=0$ | No transitions | Reduction in population by analyzer[b] |
|---|---|---|---|---|---|---|---|
| 1. | 2. | 3. | 4. | 5. | 6. | 7. | 8. |
| $a_1$ | $\frac{1}{4}$ | $\frac{1}{4}e^{-\lambda_1 t}$ | $\frac{1}{4}e^{-\lambda_3 t}$ | $\frac{1}{4}e^{-\lambda_2 t}$ | $\frac{1}{4}e^{-\lambda_1 t}$ | $\frac{1}{4}e^{-\lambda_1 t}$ | $e^{-\lambda_1' t'}$ |
| $a_2$ | $\frac{1}{4}$ | $\frac{1}{4}e^{-\lambda_2 t}$ | $\frac{1}{4}e^{-\lambda_2 t}$ | $\frac{1}{4}e^{-\lambda_2 t}$ | $\frac{1}{8}(e^{-\lambda_2 t}+e^{-\lambda_3 t})$ | $\frac{1}{4}e^{-\lambda_2 t}$ | $e^{-\lambda_2' t'}$ |
| $a_3$ | $\frac{1}{4}$ | $\frac{1}{4}e^{-\lambda_3 t}$ | $\frac{1}{4}e^{-\lambda_1 t}$ | $\frac{1}{4}e^{-\lambda_3 t}$ | $\frac{1}{4}e^{-\lambda_2 t}$ | $\frac{1}{4}e^{-\lambda_3 t}$ | $e^{-\lambda_3' t'}$ |
| $a_4$ | $\frac{1}{4}$ | $\frac{1}{4}e^{-\lambda_2 t}$ | $\frac{1}{4}e^{-\lambda_2 t}$ | $\frac{1}{4}e^{-\lambda_1 t}$ | $\frac{1}{8}(e^{-\lambda_2 t}+e^{-\lambda_3 t})$ | $\frac{1}{4}e^{-\lambda_2 t}$ | $e^{-\lambda_2' t'}$ |

[a] The $\lambda_i$ are defined by Eq. (5). Unprimed quantities refer to the polarizer, and primed quantities to the analyzer.
[b] The population surviving the analyzer may be found for the case of each of the possible transitions by multiplying the value in column eight by the appropriate value in column four, five, six, or seven.

TABLE III. Fraction of the metastable ions that contribute to the rf induced signal and background, for various transitions.

| Transition | Signal | Background[a] |
|---|---|---|
| $\Delta m_F=0$, $\Delta F=1$ | 0.069 | 0.174 |
| $\Delta m_F=\pm1$, $\Delta F=1$ | 0.048 | 0.152 |
| $\Delta m_F=\pm1$, $\Delta F=0$ | 0.0033 | 0.218 |

[a] The background depends upon the polarizer and analyzer settings. These are different for each of the transitions.

klystron is capable of supplying sufficient rf power to quench all the metastables in the beam. Rf power in the polarizer is modulated at 280 cps by superimposing a square wave on the beam voltage of the first klystron, thereby swinging the tube in and out of its principal mode. Figure 10 illustrates the state-selection circuitry.

## VI. QUENCHING AND STARK EFFECTS

The metastable ions are susceptible to a variety of adverse electric-field effects. Most serious among them is a shift in the apparent value of the hfs splitting due to electric fields in the hfs transition region, which act to mix the $2\,^2S_{\frac{1}{2}}$ state with the nearby $2P$ states. There are two sources of electric field in the transition region, the space-charge field accompanying the ion beam and the rf electric field induced by the oscillating magnetic field used to produce the hfs transitions. The space-charge effect may be estimated by consideration of the static Stark shift. The displacement of an energy level $E_m$ in the presence of an electrostatic field $\mathbf{E}$ is given by

$$\Delta E_m=\sum_n{}'\frac{|(n|e\mathbf{E}\cdot\mathbf{r}|m)|^2}{E_m-E_n}. \tag{14}$$

For the case of $He^{3+}$ the most important term is that connecting the $2\,^2S_{\frac{1}{2}}$ and $2\,^2P_{\frac{1}{2}}$ states; the $2\,^2P_{\frac{3}{2}}$ state contributes less than one percent of the total shift. From Eq. (14) we find that the static Stark shift in the separation between the $m_F=0$ levels of the hyperfine doublet is

$$\delta(\Delta\nu)=-(6.6E_\perp{}^2+8.8E_z{}^2)\text{ cycles/sec}, \tag{15}$$

where $E_\perp$ and $E_z$ are the transverse and longitudinal components of the electric field expressed in volts/cm. This formula is valid only if the Stark shift is small compared with the Zeeman splitting, but this condition is well satisfied for all cases of interest here. The beam cross section is approximately 3 cm×1 cm, but for the present purpose we can replace this by an idealized beam of the same current density whose long transverse dimension is infinite. For a current density of $10^{-8}$ amp/cm$^2$ and a beam energy of 20 ev the maximum space-charge electric field is

$$E=2\pi\sigma=0.016\text{ volt/cm}. \tag{16}$$

Thus the Stark shift from space charge is negligible. It is shown in Appendix IV that the formula for the static Stark shift [Eq. (15)] provides a very good estimate of the rf Stark effect if we replace $E_\perp$ and $E_z$ by the root-mean-square values of the oscillating field components. In the case of the separated-oscillating-field transition region the fields are not uniform, and it is difficult to make a reliable estimate of the rf electric field. However, in the case of the single oscillating-field-transition region the fields are approximately uniform and the rms field components are

$$E_\perp=\omega(H_1y/\sqrt{2}c);\quad E_z=0, \tag{17}$$

where $\omega$ is the frequency of the applied field in radians/sec, $H_1$ is the peak amplitude of the oscillating magnetic field, $y$ is the distance from the bottom of the transition region (see Fig. 13), and $c$ is the velocity of light. In Eq. (17) it is assumed that the static magnetic field is parallel to the beam axis. This condition was approximately satisfied in the actual apparatus. The oscillating field amplitude ($H_1$) may be estimated from the condition for maximum transition probability for the $\sigma$ transition [see Eq. (21)]. This is:

$$H_1=\pi\hbar v/\mu_0 L. \tag{18}$$

Here $\hbar$ and $\mu_0$ have their usual meaning, $v$ is the beam velocity, and $L$ is the length of the transition region. Inserting the foregoing value for $H_1$ into Eq. (17) we find a shift of $-39y^2$ cps at a beam energy of 20 ev. Averaging this shift over a beam height of 1.5 cm we find a net rf Stark shift of $-29$ cps for the single oscillating field transition region.

There also exists quenching of metastable ions by electric fields. The decay rate of the $2\,^2S_{\frac{1}{2}}$ state in the presence of a static field $E$ is given by

$$\gamma_S=\frac{\gamma|(2\,^2P_{\frac{1}{2}}|e\mathbf{E}\cdot\mathbf{r}|2\,^2S_{\frac{1}{2}})|^2}{\hbar^2[(\frac{1}{2}\gamma)^2+\omega_S{}^2]}, \tag{19}$$

if hfs is neglected, and also if the natural decay rate is

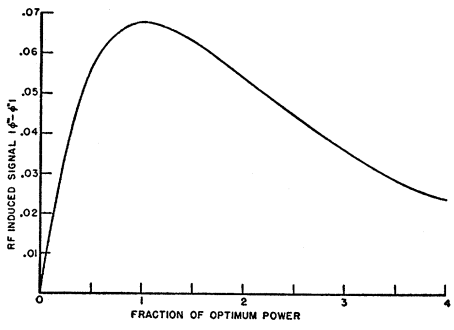


FIG. 9. Rf induced signal for the $\sigma$ transition as a function of rf power in one state selector, when the power in the other state selector is adjusted to optimum. Both state selectors are driven at 13 350 Mc/sec.

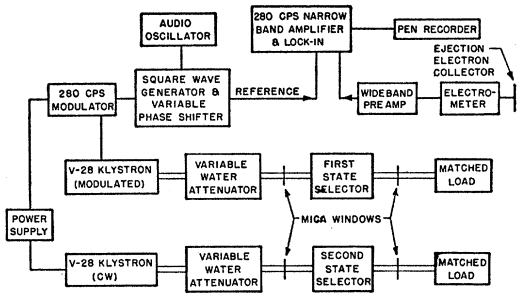


FIG. 10. Schematic diagram of the state-selection rf circuitry.

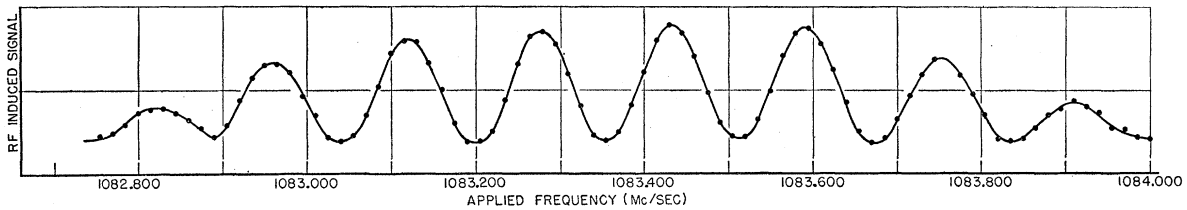


FIG. 11. Resonance curve of the $\sigma$ transition obtained with separated oscillating fields. The static and rf magnetic fields are oriented parallel, giving zero probability for $\pi$ transitions.

neglected.[20] In Eq. (19), $\gamma$ is the natural decay rate of the $2\,^2P_{\frac{1}{2}}$ state, and $\omega_S$ is the Lamb shift in radians-per-second. If hfs is included $\omega_S$ in Eq. (19) must be replaced by the appropriate separation of the $2\,^2S_{\frac{1}{2}}$ and $2\,^2P_{\frac{1}{2}}$ sublevels, and slightly different quenching rates are obtained for each of the hfs components. Thus, in particular, there is a small differential quenching as the beam is accelerated. Nevertheless, for the present purposes Eq. (19) is adequate. For $He^{3+}$,

$$\gamma_S = 63E^2 \text{ sec}^{-1}, \tag{20}$$

where $E$ is in volts/cm. This result is valid only for quenching rates that are large compared to the natural decay rate of the $2\,^2S_{\frac{1}{2}}$ state. Since the total beam transit time is only $10^{-5}$ second, the space-charge fields produce negligible quenching. Indeed, the total metastable signal has been observed to be proportional to ion current over a wide range, indicating experimentally that space-charge quenching effects are very small. Quenching may also arise from beam electrode fields; the most intense of these is the acceleration field. Here approximately 10% of the metastables are quenched on acceleration to 20 ev. The ratio of total metastable signal to ion current has been observed to be independent of pressure over a wide range, indicating that pressure quenching effects are quite small. Quenching of the metastables by the rf electric fields in the transition region is discussed in Appendix IV.

## VII. HFS TRANSITION PROBABILITIES AND LINE SHAPE

If a precision of the order of one part per million is to be achieved in the determination of $\Delta\nu$, it is desirable that the line width of the observed transition be of the order of 100 kc/sec or less. If the beam energy is 20 ev, such a line width can only be achieved with a transition region approximately 25 cm long, which is almost one wavelength at the hfs transition frequency. On the other hand, it is desirable that the rf field $H_1$ be homogeneous over the beam path length for a single oscillating field, in order that the line shape be of a known form. At the outset of this experiment it seemed difficult to reconcile the two requirements of homogeneous $H_1$ and a transition region one wavelength long in the design of a single oscillating field. For this reason, a separated-oscillating-fields transition region was chosen initially,[15] although later a satisfactory single oscillating-field design was employed.

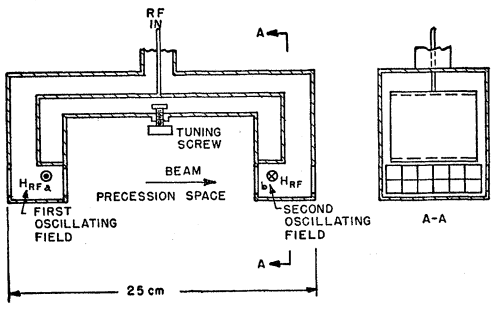


FIG. 12. Schematic diagram of the separated-oscillating-fields transition region.

The choice of separated oscillating fields avoids the difficulties we have just mentioned, because in this case the individual transition regions are quite short compared to a wavelength. Nevertheless, some special hazards are associated with the design. Since the time intervals which the beam spends in the individual oscillating fields are very short, these fields must be of the order of $\frac{1}{2}$ gauss to effect the hfs transitions. The associated rf electric fields then become of the order of 20 volts/cm. From Eq. (15) it is evident that this might result in a large Stark shift in the hfs splitting, and it is necessary to choose a design which minimizes such an effect.

A second difficulty is that although individual interference fringes are narrow, the resonance-curve envelope is relatively broad for a monoenergetic beam with separated oscillating fields (see Fig. 11). Here the envelope half-width is approximately 900 kc/sec for a 20-ev beam. As a consequence there exists the possibility of distortion of the transition line shape by overlap, or interference between the $\pi$ and $\sigma$ transitions. To avoid overlap, the $\pi$ transition intensity must be suppressed or the frequency separation between $\pi$ and $\sigma$ transitions made greater than 2 Mc/sec.

The separated-oscillating-fields structure is a $\frac{3}{2}$ wavelength shorted transmission line in which the rf current enters through the center conductor and returns via the grounded outer envelope (see Fig. 12). The intention of this design, suggested originally by Heberle, Reich, and Kusch,[10] is to minimize the rf electric field intensities in regions $a$ and $b$ of Fig. 12. The results of measurement of a transition with

[20] W. E. Lamb, Jr., and R. C. Retherford, Phys. Rev. **79**, 549 (1950).

separated oscillating fields are most easily interpreted when the rf fields in regions $a$ and $b$ are either in phase or out of phase by 180°. To reduce the electric field to a minimal value at points within the effective transition region, the out-of-phase configuration is chosen, and the beam is exposed to strong electric fields only before region $a$ and after region $b$.

The single oscillating-field design which was finally adopted is shown in Fig. 13. Here also, the rf current enters through the center conductor and returns via the grounded outer envelope. The slots in the center conductor are for the purpose of preventing the propagation of modes of oscillation other than the *TEM* mode. Thus it is intended that the electromagnetic wave propagation vector be everywhere perpendicular to the beam velocity vector in the region of the beam. The magnetic field lines are then as indicated in Fig. 13. Probe measurements show that propagation is in the desired mode, and in this way the inhomogeneities mentioned earlier in this section are largely avoided. The total beam path length here is approximately the same as in the separated-oscillating-fields transition region. However, the total time which the beam spends exposed to rf fields is much longer in the present case and much lower magnetic field intensities are required. Therefore the possibility of an rf Stark shift is much reduced. Moreover, the resonance curve envelope width is much narrower than in the case of separated oscillating fields and overlap difficulties are eliminated.

For a homogeneous single oscillating field the $\sigma$ hfs transition probability is given by

$$P_0=\frac{(2b_0)^2}{\lambda^2+(2b_0)^2}\sin^2[\tfrac{1}{2}(\lambda^2+(2b_0)^2)^{\frac{1}{2}}t]. \qquad (21)$$

Here, $\lambda=\omega-\omega_0$ where $\omega$ is the applied frequency, $\omega_0$ is the resonant frequency, both in radians/sec, $t$ is the time spent in the transition region, and

$$b_0=(\mu_0/4\hbar)(g_J-g_I)H_1\cos\theta,$$

where $\theta$ is the angle between static and rf magnetic fields, $H_1$ is the peak amplitude of the oscillating rf field and $\mu_0$, $\hbar$, $g_J$, and $g_I$ have their usual meanings. From Eq. (21) and Fig. 14 it can be seen that the central fringe of the resonance curve narrows for a monoenergetic beam when the rf power is above

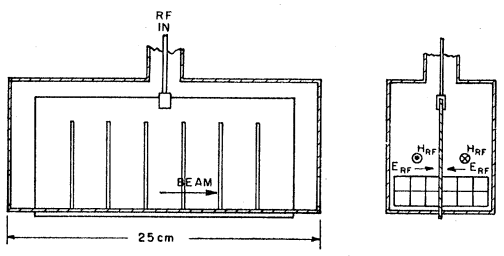


FIG. 13. Schematic diagram of the single oscillating-field transition region.

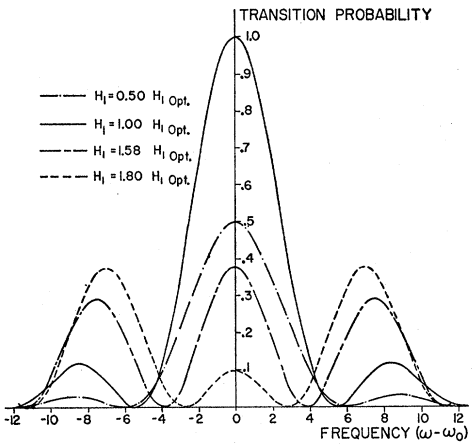


FIG. 14. Theoretical transition probability as a function of applied frequency, for a homogeneous single oscillating field and a monoenergetic beam [Eq. (21)]. Curves corresponding to several different rf power levels are plotted.

optimum. At the same time the intensity of the central maximum decreases and the intensities of the side maxima increase. This effect has been observed experimentally (see Fig. 15). It is to be contrasted to the case of conventional molecular beams where the right-hand side of Eq. (21) must be integrated over the Maxwellian distribution to give the line shape.[21] In that case, broadening of the line occurs as the rf power is increased above optimum. Finally, it has been observed experimentally that the subsidiary maxima are more intense at optimum rf power than one would expect from Eq. (21). An explanation lies in the fact that the rf field is not perfectly homogeneous, but as shown by probe measurements, is slightly stronger toward the ends of the transition region than in the middle. A calculation of the line shape shows that such a field distribution does in fact cause this change.[22] (Since the change is symmetrical, no shift in resonance is to be expected; an experimental search for phase-shift effects was made by taking data with two different orientations of the oscillating-field structure.)

Although the rf field in the single oscillating-field structure is much smaller than in the separated-oscillating-fields structure, approximately ten watts are required to drive each. A Collins 32-V-3 transmitter was employed as the frequency source. It supplies a tunable signal in the neighborhood of 30 Mc/sec which is stable to better than one part in $10^7$. This frequency is multiplied by a factor of 36 by a multiplier chain whose output (in the neighborhood of 1080 Mc/sec), drives a Sperry type SAL 39 klystron amplifier. The gain of this amplifier may be controlled by varying its beam-supply voltage, and it is capable of providing more than 100 watts CW to the hfs transition region. Unfortunately, the SAL 39 klystron is intended for

[21] H. C. Torrey, Phys. Rev. **59**, 293 (1941).

[22] We are indebted to Professor N. F. Ramsey for carrying out this calculation for us on an electronic computer.

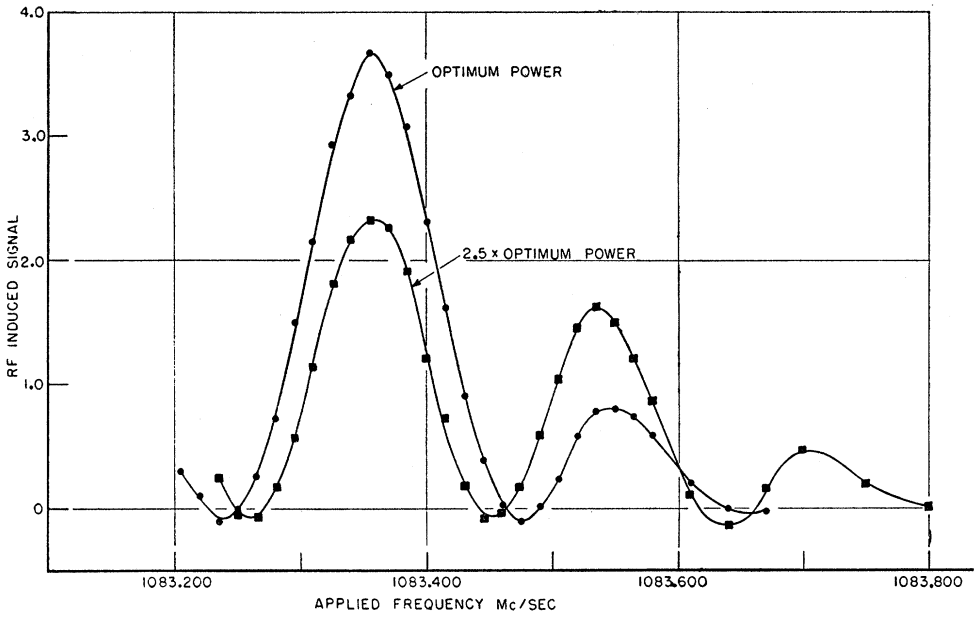


FIG. 15. Resonance curves of the $\sigma$ transition obtained with the single oscillating field for two distinct rf power levels.

pulse operation, and use of the tube as a CW amplifier involved a number of difficulties. At high beam voltages it has a tendency to oscillate, although this may be prevented by placing a small magnet near the output cavity. Also if one uses ac on the klystron heaters the rf output exhibits approximately 10% modulation at 120 cps. Use of a dc heater supply avoids this difficulty, but this is rather inconvenient since 45-amperes heating current is required. The band width of the klystron is narrow, and the tube must be retuned for optimum power output at intervals of approximately $\frac{1}{2}$ Mc/sec. The band width of the single oscillating-field structure is extremely broad, while that of the separated-oscillating-fields structure is approximately 15 Mc/sec. The latter is therefore provided with a capactive tuning screw (see Fig. 12). Figure 16 illustrates the details of the rf circuitry. Finally, the rf-induced signal has been observed as a function of applied power in order to determine optimum operating conditions. Figure 17 illustrates data taken with the separated oscillating fields. Since the ion beam is monoenergetic the curve has the shape of the function $\sin^2(P^{\frac{1}{2}})$ as expected.

## VIII. DETECTION

Two of a number of possible methods were employed for detecting the hfs transitions. In the photoelectric detector, which was used for preliminary data, Lyman-alpha radiation emitted during the decay of metastables in the analyzer passes through a system of grids and falls on a semicylindrical platinum photo surface. The photoelectrons are collected by a positively biased pickup wire and the current is fed to an electrometer followed by a galvanometer. The first of the grids is merely one side of the analyzer wave guide, perforated to allow passage of the light. A second grid supports an aluminum film of thickness 500 A, which serves to prevent charged particles from entering the detector region. The transmission of this film for 300-A light is approximately 50%.[23] In order to estimate the signal strength to be expected from the photodetector, we use Eq. (11). For the present apparatus,[24] $T=\frac{1}{8}$, $\eta=0.03$ and $\Omega/4\pi=0.05$. For $\sigma$ transitions, $|\phi'''-\phi''|=0.069$ and $I_{2S}{}^0=2\times10^{-10}$ amp for an ion current of $2\times10^{-8}$ ampere. Inserting these factors in Eq. (11), we have

$$|S_p|=2.6\times10^{-15} \text{ ampere.} \qquad (22)$$

The photodetector has the advantage that undesirable background may be reduced to a very low level by means of the film and the grids. Moreover, the associated electronic equipment is extremely simple. Unfortunately, as indicated by Eq. (22), the signals obtainable with this detector are quite small, and it was ultimately abandoned in favor of the surface ejection method.

Detailed studies of the ejection of electrons from metal surfaces by singly and doubly charged helium ions have been carried out by Hagstrum.[25] He has shown that the electron yields from molybdenum for slow $He^+$ ground-state ions and for slow $He^{++}$ ions are: $\gamma_{1S}{}^+=0.30$ and $\gamma^{++}=0.81$, respectively. Hagstrum has pointed out further that the yields for metastable ions and for double ions should be comparable. Finally, he has shown that when the ejection surface is atomically clean, the maximum electron energy should be given by: $E_e=W_i-2\phi$, where $W_i$ is the excitation energy of the

[23] D. H. Tomboulian and D. E. Bedo, Rev. Sci. Instr. **26**, 747 (1955).
[24] W. C. Walker (private communication).
[25] H. D. Hagstrum, Phys. Rev. **104**, 309 (1956); **104**, 672 (1956); also private communication.

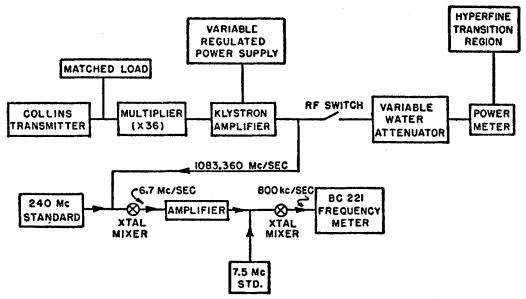


FIG. 16. Schematic diagram of the hfs transition rf circuitry.

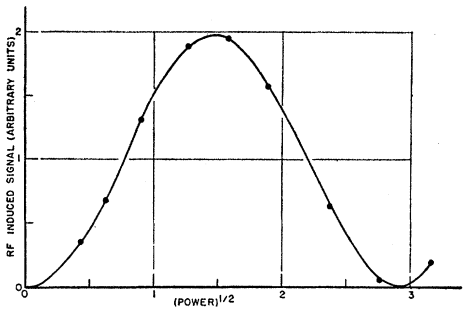


FIG. 17. Rf-induced signal for the $\sigma$ transition, plotted as a function of applied rf magnetic field in the hfs transition region. The data were taken with separated oscillating fields.

ion, and $\phi$ is the work function of the metal surface. For ground-state ions, $E_e(1S)=25$ ev$-2\phi$. For metastable ions the neutralization presumably occurs in a two-step process. First the metastable ion decays to the ground state, with the accompanying ejection of an electron of energy $E_e(2S)=40$ ev$-2\phi$. The second step of the process is the neutralization of the resulting ground-state ion.

Originally, efforts were made to discriminate by means of retarding potentials against the low-energy electrons ejected with neutralization of the ground-state ion. However, unfavorable geometry and surface contamination prevented this. Therefore a large background exists due to ground-state ions, constituting the chief disadvantage of surface ejection, and it is necessary to use a narrow-band detection scheme to circumvent the difficulty. The metastable component of the beam and hence the electron current is modulated at 280 cps (see Sec. V). This modulated electron current is fed into an electrometer, followed by a wide-band preamplifier and a Numar Type 104 narrow-band amplifier and lock-in detector. The output is applied to a pen recorder.

We again refer to Sec. V in order to estimate the signal, background, and noise of this detector. Inserting $|\phi'''-\phi''|=0.069$, $I_{2S}{}^0=2\times10^{-10}$ amp, $\gamma_{2S}{}^+=0.81$ and $\gamma_{1S}{}^+=0.30$ in Eq. (9), we find

$$|S_S|=7.0\times10^{-12} \text{ ampere.}$$

Inserting $|\phi''-\phi'|=0.174$ and the values of $\gamma_{1S}{}^+$, $\gamma_{2S}{}^+$, and $I_{2S}{}^0$ listed above in Eq. (10), we find

$$B_S=1.8\times10^{-11} \text{ ampere.}$$

A theoretical calculation of the noise inherent in the ejection current is difficult. However, it may be assumed that this arises principally from the fluctuations in the 280-cps component of the electron current ejected by ground-state ions. Then the noise current is given by

$$(I_n)^2=2eI_{1S}\beta\gamma_{1S}{}^+(1+\gamma_{1S}{}^+),$$

where $\beta$ is the band width of the lock-in detector, $I_{1S}$ is the ion current, and $e$ is the electronic charge in coulombs. For an ion current of $2\times10^{-8}$ ampere, for $\gamma_{1S}{}^+=0.3$ and for $\beta=0.1$ sec$^{-1}$, we have $I_n=1.6\times10^{-14}$ amp. This gives a signal-to-noise ratio of approximately 440. If the electron current were observed at the ion collector electrode directly, the full 280-cps shot-noise of the ion beam would be present in the signal, and the estimated signal-to-noise ratio would be reduced by a factor of 1.8. The advantage of the present arrangement of electrodes is apparent rather than real, however, since noise in the ion source and in the detector limited the actual signal-to-noise ratio to about forty.

## IX. VACUUM SYSTEM

Special precautions have been taken to prevent instabilities in the ion current resulting from the electrical charging of insulating films on the surfaces exposed to the beam. The vacuum system is constructed of type-304 stainless steel and is equipped with mercury diffusion pumps. Provision is made for baking the main chamber at 300°C and all seals on this chamber are made with gold or copper gaskets in an effort to eliminate the possibility of organic contamination. No instabilities in the ion current were experienced as long as all of these precautions were observed. On one occasion when the system was not baked out there was definite evidence of beam instability. It was observed that after 200 hours of operation the surface of the electron collector in the ion source was nearly as clean as when it was first installed. This is in strong contrast to the usual experience with kinetic vacuum systems where blackening is observed after a few hours of operation.[26] Ultimate vacua of $3\times10^{-8}$ mm Hg were obtained. $He^3$ was recirculated continuously and purified with a charcoal trap immersed in liquid nitrogen. The gas sample, obtained from the U. S. Atomic Energy Commission, was of Type M-1.

## X. OBSERVATIONS

### A. Zeeman Effects

The zero-field hfs splitting $\Delta\nu_0$ is determined from observations of the $\sigma$ transition in a weak static magnetic field by applying a quadratic Zeeman correction to

[26] For a discussion of organic contamination of kinetic vacuum systems, see A. E. Ennos, Brit. J. Appl. Phys. 5, 27 (1954).

the observed resonant frequency. The static field must be sufficiently intense to give adequate separation of the $\sigma$ and $\pi$ transitions; otherwise the resonances are shifted by overlap effects. However, excessively large static-field values make possible substantial uncertainties in the quadratic correction. Since in the case of the separated-oscillating-fields transition region the width of the resonance envelope is 900 kc/sec, overlap effects can only be avoided by using fields of more than 2 gauss, if the $\pi$ and $\sigma$ transitions have comparable intensities. In order to avoid such high fields, the $\pi$ resonance amplitude is made very much smaller than the $\sigma$ amplitude by orienting the static field parallel to the rf field. There then remains the problem of determining the static-field strength when the $\pi$ transition probability is close to zero. A rather indirect procedure was adopted. Initially the residual field was determined roughly by flip-coil measurements at various positions along the beam trajectory. It was found that the axial component ($z$-component) was very much smaller than the $x$- and $y$-components. External rectangular coils to compensate the $x$- and $y$-components were placed symmetrically with respect to the beam axis, and the $\Delta m=-1$ transition was observed for a number of coil current settings and at several field angles. In this way the average field-per-unit current which each coil generates was determined, i.e., the coils were calibrated. This was done on two separate occasions and between these the main body of separated-oscillating-fields data was taken. For one set of coils the agreement of the two separate calibrations was within $\frac{1}{3}\%$ and for the other it was within $\frac{1}{10}\%$. Since the residual field fluctuates from day to day it was necessary, in addition, to observe the $\Delta m=-1$ transition before and after each daily group of $\sigma$ transitions. In this way the mean daily $x$- and $y$-residual components were determined. The $z$-component contributed an insignificant amount to the total static field, and could be neglected. Finally, for observation of the $\sigma$ transition, the static field was oriented parallel to the rf magnetic field, giving zero probability for the $\pi$ transitions. The Zeeman correction was then determined from the observed residual fields and coil current settings. It is estimated that the correction was obtained to within 2%. A typical value of the Zeeman correction was 1.40 kc/sec.

A simpler procedure could be adopted in the case of the single oscillating field, since the line width is only 110 kc/sec for a 20-ev beam. Here the $\pi$ and $\sigma$ transitions were observed for the same coil settings and the difference in their resonance frequencies was used to find the quadratic correction directly. In this case the rf magnetic field was parallel to the beam axis, and it was necessary to apply an axial static field with an additional set of coils. The ratio of $\sigma$ to $\pi$ amplitudes was about 5:1 for the single oscillating field.

### B. Observation of $\sigma$ Transitions

All final observations were made with the surface ejection detector. In these data, a single determination of the transition consisted in observing the transition intensity at 10 to 12 frequencies on either side of the midpoint of the central resonance fringe. The following procedure was adopted:

1. With the hfs transition rf field off, the polarizer and analyzer rf fields off, and the beam running, a base line trace was established on the recorder chart. Fluctuations of this trace from a straight line were attributed to detector noise plus the beam noise in a narrow band about 280 cps. With the hfs transition rf power still off, but the modulated polarizer field and the analyzer field now on, a deflection was observed which was proportional to the metastable beam background. The level of this background could be adjusted to any fraction of the total metastable beam signal by setting the polarizer and analyzer power levels. The optimum settings for various transitions were determined from values in Table III.
2. The Collins transmitter was set at a predetermined frequency and the hfs transition rf was turned on. An rf-induced signal was then exhibited as a displacement of the recorder trace from the background level. The time for the trace to come to equilibrium was entirely determined by the lock-in detector time constant, which was twenty seconds.
3. The displacements for four separate frequencies were observed consecutively in this manner. A pair of observations was always made on one side of the line and then a second pair on the other, to compensate for instrumental drifts.
4. The rf was then turned off and the background trace was re-established in order to observe if any drifts had actually occurred.
5. In reduction of the data the two successive positions of the background trace were connected by a straight line segment, and the rf-induced signal was the measured distance of the equilibrium trace for a given frequency from the interpolated background line. Usually fluctuations of the background trace were no greater than one tenth of a millivolt on the Leeds and Northrop recorder, while the maximum rf-induced signal was usually from two to four millivolts.
6. Frequency measurement was by a heterodyne method. The ninth harmonic of 240 Mc/sec from a frequency standard was compared with the second harmonic of the output from the SAL 39 klystron amplifier. The difference between these two frequencies, approximately 6.7 Mc/sec, was compared with 7.5 Mc/sec from the frequency standard. The difference in these two frequencies was observed with a BC 221 frequency meter. The frequency standard was compared daily with WWV. The BC 221 was calibrated with 10 kc/sec markers from the frequency standard.

### C. Resonance Distortion Effects

Several effects might cause shifts and distortion of the resonance. Aside from overlap and rf Stark shift, which have already been discussed, there exist the possibilities of pressure effects, phase shifts in the oscillating field, and variations in oscillating-field strength as a function of frequency. To determine phase-shift effects observations were made with the transition region oriented first in one position and then in the reverse position. A search was made for an rf Stark shift by observing the resonance at several different power levels. Overlap effects were investigated by observation of $\Delta\nu$ at different beam voltages and static magnetic field values.

### D. Final Data

Eighty-six separate determinations of $\Delta\nu$ were made. Of these, 68 were made with the separated oscillating fields and the remainder with the single oscillating field. These determinations fall into twelve distinct groups. Each corresponds to a unique set of experimental conditions, chosen to allow investigation of possible resonance shifts of the kind discussed in Sec. XC. An elaboration of these conditions is given in Table IV; for example, groups 1–5 were taken with one orientation of the separated oscillating fields and groups 6–8 with this structure reversed.

All of the data were reduced by a two-point interpolation method. In addition, some of the data obtained with the separated oscillating fields were reduced by fitting a least-squares cosine curve to the observed points. The arithmetic means of the determinations in each group are plotted in Fig. 18, together with their statistical probable errors, for each method of reduction. Finally, the two-point interpolation data were divided into two groups corresponding to the upper and lower halves of the resonance curves, in order to investigate possible asymmetries. The arithmetic means of the data using these different reductions are listed in Table IV.

TABLE IV. Summary of observations.[a]

| Group[b] | (a) | (b) | (c) | (d) | (e) | (f) |
|---|---|---|---|---|---|---|
| 1 | 9 | 10 | $2.4\times10^{-5}$ | 1.40 | $\alpha$ | $A$ |
| 2 | 10 | 20 | $2.4\times10^{-5}$ | 1.39 | $\alpha$ | $A$ |
| 3 | 10 | 10 | $2.4\times10^{-5}$ | 2.68 | $\alpha$ | $A$ |
| 4 | 10 | 20 | $2.4\times10^{-5}$ | 2.66 | $\alpha$ | $A$ |
| 5 | 4 | 20 | $2.4\times10^{-5}$ | 2.68 | $\beta$ | $A$ |
| 6 | 13 | 20 | $2.4\times10^{-5}$ | 1.38 | $\alpha$ | $B$ |
| 7 | 7 | 20 | $2.4\times10^{-5}$ | 1.40 | $\beta$ | $B$ |
| 8 | 5 | 20 | $1.4\times10^{-5}$ | 1.41 | $\alpha$ | $B$ |
| 9 | 5 | 20 | $2.4\times10^{-5}$ | 1.36 | $\alpha$ | $A$ |
| 10 | 5 | 20 | $2.4\times10^{-5}$ | 1.41 | $\alpha$ | $B$ |
| 11 | 4 | 20 | $2.4\times10^{-5}$ | 1.40 | $\beta$ | $B$ |
| 12 | 4 | 20 | $0.9\times10^{-5}$ | 1.40 | $\alpha$ | $B$ |

| Group | (g) | (h) | (i) | (j) | (k) | (l) |
|---|---|---|---|---|---|---|
| 1 | 1 083 354.72 | 4.91 | 4.51 | | 0.14 | |
| 2 | 5.18 | 5.15 | 5.29 | | 0.16 | |
| 3 | 4.91 | 4.85 | 4.98 | | 0.12 | |
| 4 | 5.13 | 5.01 | 5.26 | 4.91 | 0.08 | 0.07 |
| 5 | 5.07 | 5.06 | 5.03 | | 0.20 | |
| 6 | 4.82 | 4.82 | 4.82 | 4.90 | 0.04 | 0.04 |
| 7 | 5.12 | 5.00 | 5.27 | 5.24 | 0.15 | 0.13 |
| 8 | 4.65 | 4.61 | 4.70 | 4.66 | 0.06 | 0.10 |
| 9 | 5.00 | 4.91 | 5.08 | | 0.04 | |
| 10 | 5.23 | 5.12 | 5.34 | | 0.08 | |
| 11 | 5.13 | 5.36 | 4.92 | | 0.22 | |
| 12 | 5.18 | 5.04 | 5.32 | | 0.07 | |
| Group mean values: | 5.01 | 4.99 | 5.04 | 4.94 | | |

Arithmetic mean of 86 separate observations: 1 083 354.99 kc/sec

[a] The items in the columns refer to:

(a) Number of determinations in a group.
(b) Ion beam energy, ev.
(c) Pressure, mm Hg. These pressures were observed with an ionization gauge calibrated for nitrogen.
(d) Zeeman correction, kc/sec.
(e) Rf power. For those entries marked $\alpha$, the rf power was set for optimum transition probability. For those entries marked $\beta$, the rf power was set for $\frac{1}{2}$ of optimum.
(f) Orientation of hfs transition region. For those entries marked $A$ the transition region was in one position; for those marked $B$ this position was reversed.
(g) Arithmetic mean of data as reduced by two-point interpolation; kc/sec.
(h) Arithmetic mean of upper halves of resonance curves; data reduced by two-point interpolation; kc/sec.
(i) Arithmetic mean of lower halves of resonance curves; data reduced by two-point interpolation; kc/sec.
(j) Arithmetic mean of $\Delta\nu$ as determined from data reduced by fitting resonance curve to a least-squares cosine curve; kc/sec.
(k) Statistical probable error of interpolated mean, kc/sec.
(l) Statistical probable error of values of $\Delta\nu$ obtained by fit of cosine curve; kc/sec.

[b] Groups 1–8 were obtained with the separated oscillatory field type of transition regions, groups 9–12 with the single oscillatory field type of transition region.

### E. Uncertainties

The statistical probable error of the arithmetic mean of all 86 determinations is 36 cps. However, this cannot be used as a measure of the uncertainty of the final result, since allowance must be made for uncertainties in various systematic effects. It is estimated that all of the frequency readings might be in error by as much as 25 cps, due to inaccuracies in calibrating the BC 221 and setting it to zero-beat. Since the sign of this effect is not known, it contributes in its entirety to the final uncertainty. The difference between the upper and lower means is 50 cps. This difference might arise from frequency sensitivity of the rf circuits and rf power monitor. An allowance of 25 cps is made in the final uncertainty for this effect. The sum of the above uncertainties is 86 cps.

### F. Corrections

The Bloch-Siegert correction,[27] the transverse Doppler shift, and the magnetic field inhomogeneity correction are each a few cycles-per-second and may be neglected. If the data are extrapolated to zero rf power, the apparent value of the hfs splitting is $\Delta\nu=1083.35511$ Mc/sec, indicating the possibility of an rf power shift of $-120$ cps. The earlier estimate of the rf Stark effect indicates that a power shift of $-29$ cps might

[27] F. Bloch and A. Siegert, Phys. Rev. **57**, 522 (1940).

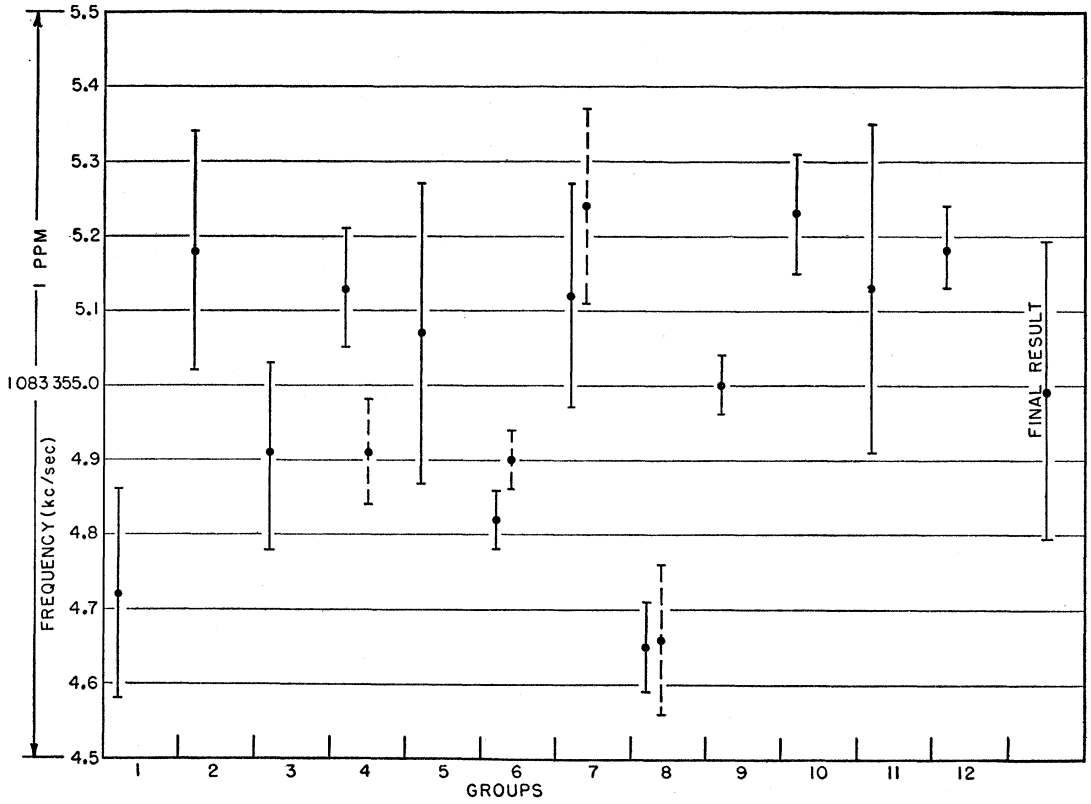


FIG. 18. Arithmetic means of 86 separate determinations of $\Delta\nu$, as arranged in 12 distinct groups, each corresponding to a unique set of experimental conditions. The vertical lines indicate the statistical probable error of each group of determinations. The final value of $\Delta\nu$, together with its estimated uncertainty, is plotted at the extreme right of the figure. The points with uncertainties indicated by dotted lines are associated with the cosine curve reduction. (See Table IV.)

be expected. Extrapolation of the data to zero pressure indicates the possibility of a pressure shift of +200 cps. Presumably such an effect could arise from the collision of metastable ions with the residual gas in the vacuum envelope. Such collisions might be expected to mix $P$ states with the $2\,^2S_{\frac{1}{2}}$ state and so reduce the apparent hfs splitting. Thus the apparent "pressure shift," obtained by extrapolation, has the wrong sign.

However, an analysis of variance supports the assumption that both these apparent "shifts" are within the statistical fluctuations of the data. Thus no correction is made for these effects, but the final uncertainty is chosen to include their possibility.

### G. Final Result

The final result is

$$\Delta\nu(\mathrm{He}^{3+},\ 2\,^2S_{\frac{1}{2}}) = 1083.35499 \pm 0.00020 \text{ Mc/sec.} \quad (23)$$

## XI. CONCLUSIONS

### A. Nuclear Structure Effects

A theoretical estimate of $\Delta\nu$ for a point-dipole nucleus is given by the following expression:

$$\Delta\nu_p = [(16/3)\alpha^2 R_\infty c(\mu_{\mathrm{He}^3}/\mu_{\mathrm{H}^1})(\mu_{\mathrm{H}^1}/\mu_s)(\mu_s/\mu_0)] \times[1-3m/M_{\mathrm{He}^3}]\times[1+(17/2)\alpha^2] \times[1+\alpha/2\pi-0.328\alpha^2/\pi^2]\times[1-2\alpha^2(5/2-\ln 2)]. \quad (24)$$

The first quantity in brackets is obtained from the simple Fermi formula.[28] The ratio of the $He^3$ nuclear moment to the Bohr magneton is most precisely determined by the product of three factors (in parentheses): the ratio of the nuclear moments of $He^3$ and $H^1$,[29,30] the ratio of the $H^1$ nuclear moment to the spin moment of the electron,[31] and the theoretical value of the ratio of the electron spin moment to the Bohr magneton.[32] The second and third quantities in brackets are, respectively, the Breit-Meyerott reduced-mass correction[33] and the Breit relativistic correction.[34] The fourth is the anomalous-moment correction for the

[28] E. Fermi, Z. Physik **60**, 320 (1930).
[29] H. L. Anderson, Phys. Rev. **76**, 1460 (1949).
[30] For a discussion of the diamagnetic corrections in the determination of the $He^3$–$H^1$ moment ratio, see N. F. Ramsey, Phys. Rev. **78**, 699 (1950).
[31] Koenig, Prodell, and Kusch, Phys. Rev. **88**, 191 (1952).
[32] C. M. Sommerfield, Phys. Rev. **107**, 328 (1957).
[33] G. Breit and R. E. Meyerott, Phys. Rev. **72**, 1023 (1947).
[34] G. Breit, Phys. Rev. **35**, 1447 (1930).

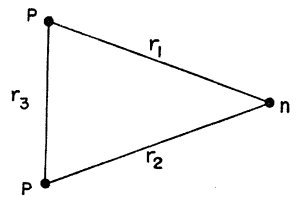


FIG. 19. Prolate spheroidal coordinates.

electron, and the fifth is the second-order radiative correction.[35] Radiative corrections of relative order $Z^2\alpha^3$, $Z\alpha^3$, and $\alpha^3$ are believed to exist; however, these have not as yet been evaluated. Equation (24) allows for the finite nuclear mass only through the reduced-mass correction, but it does not include radiative reduced-mass corrections.[36–38] If we insert DuMond and Cohen's values for $c$ and $R_\infty$,[39] Sommerfield's value for $\alpha$,[32] and Wapstra's value for the mass of $He^3$,[40] we obtain

$$\Delta\nu_p = 1083.556 \pm 0.010 \text{ Mc/sec.} \quad (25)$$

The uncertainty in $\Delta\nu_p$ arises mostly from that in $\alpha$; it does not include any allowance for the unevaluated theoretical terms discussed in the foregoing. We introduce a quantity $\delta$ defined by

$$\Delta\nu = \Delta\nu_p(1-\delta). \quad (26)$$

Using the present experimental value for $\Delta\nu$ and the above value for $\Delta\nu_p$, we obtain

$$\delta = 186 \pm 9 \text{ ppm.} \quad (27)$$

This anomaly presumably arises from the effects of nuclear and nucleon structure, nuclear interaction currents, and unevaluated higher order radiative corrections. The structure and interaction current effects have been estimated by Sessler and Foley, while the nucleon structure contribution has been considered by Sessler and Mills.[41] If higher order radiative corrections are ignored, the anomaly $\delta$ may be expressed as follows:

$$\delta = -(\Delta_{ss} + \Delta_D + \Delta_{IC} + \Delta_{\text{nad}} + \Delta_N). \quad (28)$$

The main contribution to $\delta$ is the first term $\Delta_{ss}$, the so-called "neutron-spin $S$-state hfs anomaly in the adiabatic approximation." This is given by

$$\Delta_{ss} = -2\left(\frac{\mu_n}{\mu_{He^3}}\right)\int (r_1+r_2)\psi_N^2 d\tau \Big/ a_0 \int \psi_N^2 d\tau. \quad (29)$$

This expression is derived with an electronic wave function in the neighborhood of the nucleus which may be determined explicitly as the solution of the Schrödinger equation in prolate spheroidal coordinates (see Fig. 19). Also, $\psi_N$ is the nuclear wave function, $\mu_n$, $\mu_{He^3}$ are the magnetic moments of the neutron and the $He^3$ nucleus, respectively, and $a_0$ is the Bohr radius. The second term of Eq. (28) is the correction which results from nuclear orbital effects in the non-adiabatic approximation. The third term gives an interaction-current contribution; two forms have been discussed by Sessler and Foley. The first contributes $-2.0$ ppm to the anomaly, while the second contributes $-230$ ppm. However, results of measurements of the hfs of tritium would seem to exclude large interaction-current effects, so that in what follows we shall explicitly assume the first value for $\Delta_{IC}$. The fourth and fifth terms are a nonadiabatic correction to $\Delta_{ss}$ and a nucleon structure correction, $\Delta_N$, respectively. Evaluating the second and fourth terms with the Pease-Feshbach nuclear wave function, and inserting $\Delta_N = -1.5\times10^{-5}$, we have[41]

$$\delta = -(\Delta_{ss} - 2\times10^{-6}).$$

The values of $\delta$ for various nuclear wave functions are presented in Table V. The Pease-Feshbach function is derived by a variational method assuming Yukawa-shaped central and tensor wells, while the parameters are chosen to fit two-body data.[42] The function constructed by Kikuta, Morita, and Yamada[43] assumes a central interaction with a hard repulsive core. Two separate forms are considered: one in which the attractive part of the interaction is exponential, and the other in which it is Yukawa-shaped. The parameters are chosen to fit the two-body data, and the anomaly is computed for two different values of the singlet $n$-$p$

TABLE V. Binding energy differences and hfs anomalies as computed with various helium-three nuclear wave functions.

| Wave function | Singlet effective range $r_0$ $10^{-13}$ cm | Hard-core radius $D$ $10^{-13}$ cm | Binding energy difference Mev | $\delta$ ppm |
|---|---|---|---|---|
| Pease-Feshbach | | 0.0 | 1.041 | 155 |
| KMY exponential | 2.7 | 0.0 | 0.986 | 144 |
| | | 0.2 | 0.810 | 162 |
| | | 0.4 | 0.729 | 176 |
| | | 0.6 | 0.676 | 179 |
| KMY exponential | 2.4 | 0.0 | 1.037 | 136 |
| | | 0.2 | 0.845 | 155 |
| | | 0.4 | 0.777 | 159 |
| | | 0.6 | 0.723 | 166 |
| KMY Yukawa | 2.7 | 0.0 | 1.246 | 113 |
| | | 0.2 | 0.799 | 162 |
| | | 0.6 | 0.679 | 177 |
| KMY Yukawa | 2.4 | 0.0 | 1.358 | 105 |
| | | 0.2 | 0.865 | 151 |
| | | 0.6 | 0.723 | 167 |
| | Experimental values[a] | | 0.764 | 186±9 |

[a] See reference 44.

[35] N. M. Kroll and F. Pollack, Phys. Rev. **86**, 876 (1952).
[36] R. Arnowitt, Phys. Rev. **92**, 1002 (1953).
[37] W. Newcomb and E. Salpeter, Phys. Rev. **97**, 1146 (1955).
[38] A. C. Zemach, Phys. Rev. **104**, 1771 (1956).
[39] E. Cohen, *et al.*, Revs. Modern Phys. **27**, 363 (1955).
[40] A. H. Wapstra, Physica **21**, 367 (1955).
[41] A. M. Sessler and R. L. Mills (private communication).
[42] R. L. Pease and H. Feshbach, Phys. Rev. **88**, 945 (1952).
[43] Kikuta, Morita, and Yamada, Progr. Theoret. Phys. (Japan) **15**, 222 (1956). Also, M. Morita (private comminication).

effective range $r_0$, and several values for the hard-core radius $D$.

The table also gives values of the binding-energy difference $E$ between $He^3$ and tritium, as computed for each of the wave functions. It can be seen that nonzero values of the hard-core radius give relatively good values of $E$, while the Pease-Feshbach function is in error by 25% in its prediction of this quantity.[44] On the other hand, most of the predicted hfs anomalies are somewhat lower than the experimental value. These differences might be accounted for by interaction-current effects and radiative effects.

### B. Hfs Splitting of the Ground State of $He^{3+}$

An estimate of the hfs splitting of the ground state of $He^{3+}$ is given by the expression:

$$\Delta\nu(He^{3+}, 1\,^2S_{\frac{1}{2}}) = 8\Delta\nu(He^{3+}, 2\,^2S_{\frac{1}{2}}) \times[1-(\tfrac{5}{8})Z^2\alpha^2][1-AZ^2\alpha^3]. \quad (30)$$

The first factor in brackets is the Breit relativistic correction,[34] and the second is a radiative correction calculated by Mittelman,[45] who gives $A=5.28$. This formula has been compared with experiment in the case of hydrogen by Heberle, Reich, and Kusch.[10] These authors find an apparent value of $A=3.4\pm0.8$. The source of this discrepancy is not known. For the purpose of estimating the ground-state splitting of the $He^3$ ion we will take $A=4.04\pm1.24$. Thus we find:

$$\Delta\nu(He^{3+}, 1\,^2S_{\frac{1}{2}}) = 8665.628\pm0.013 \text{ Mc/sec}. \quad (31)$$

The uncertainty arises principally from the uncertainty in the coefficient $A$.

### C. Atomic Wave Function for the $2\,^3S_1$ State of the $He^3$ Atom

Sessler and Foley[1] have shown that the hfs splitting of the $2\,^3S_1$ state of the $He^3$ atom is related to the splitting in the ion by

$$\frac{\Delta\nu(2\,^3S_1, \text{atom})}{\Delta\nu(2\,^2S_{\frac{1}{2}}, \text{ion})} = \frac{3}{16}D(0)\left[1+\left(\Delta_{\text{rel}}-\frac{17}{2}\alpha^2\right) +\Delta_{dm}+(\Delta_{\alpha m/M}-\bar{\Delta}_{\alpha m/M})\right], \quad (32)$$

where $\Delta_{\text{rel}}$ and $\Delta_{dm}$ are relativistic and diamagnetic corrections for the $2\,^3S_1$ state of $He^3$, $\Delta_{\alpha m/M}$ and $\bar{\Delta}_{\alpha m/M}$ are relativistic reduced mass corrections for the atom and ion respectively, and $D(0)$, the electronic charge density at the nucleus of the $2\,^3S_1$ state of the atom, is defined by

$$D(0)=8\pi a_0^3\int|\psi(\mathbf{r}_1,0)|^2 dv(\mathbf{r}_1). \quad (33)$$

Here $\psi(\mathbf{r}_1,\mathbf{r}_2)$ is the nonrelativistic wave function for an infinitely heavy nucleus, and $a_0$ is the Bohr radius. The large nuclear structure corrections discussed in Sec. XI $A$ do not appear in Eq. (32) because the atomic electrons act essentially independently in producing the hyperfine splitting of the $2\,^3S_1$ state.[1] Sessler and Foley have estimated the relativistic and diamagnetic corrections. They find

$$\Delta_{\text{rel}}=5.91\alpha^2, \quad \Delta_{dm}=4.3\times10^{-6}. \quad (34)$$

No estimate has been made of the mass corrections $\Delta_{\alpha m/M}$ and $\bar{\Delta}_{\alpha m/M}$, but they are likely to be of the same order of magnitude, and of the same sign. Neglecting their difference and inserting the observed values of the splittings and the above relativistic and diamagnetic corrections into Eq. (32), we find

$$D(0)=33.1837\pm0.0007. \quad (35)$$

This quantity can be used to test proposed wave functions for the $2\,^3S_1$ state of the $He^3$ atom. Teutsch and Hughes[6] have evaluated $D(0)$ for a number of proposed wave functions. The most accurate function that they consider is a six-term Hylleraas function. For this function they find

$$D(0)=33.163\pm0.023. \quad (36)$$

Here the uncertainty in $D(0)$ is estimated from the discrepancy between the computed and observed binding energy of the $2\,^3S_1$ state. More recently, Traub and Foley[46] have computed $D(0)$ for a six-parameter wave function and also for a 12-parameter wave function. They find

$$\begin{aligned} D(0)&=33.18456, \quad 6 \text{ parameters};\\ D(0)&=33.14795, \quad 12 \text{ parameters}. \end{aligned} \quad (37)$$

The twelve-parameter function gives a value of the energy of the $2\,^3S_1$ state which is in better agreement with experiment, however.

## XII. ACKNOWLEDGMENTS

We gratefully acknowledge the invaluable aid and support given to us by Professor P. Kusch throughout this experiment. We are indebted to Professor N. M. Kroll and Professor H. M. Foley for many helpful discussions, and to Dr. J. Heberle for originally suggesting the method of rf state selection in the case of $He^3$. We wish to thank Dr. H. Hagstrum for much useful information on surface ejection phenomena. The staff of the Columbia Radiation Laboratory, in particular I. Beller, A. Costello, C. Dechert, and A. Deery, gave invaluable assistance. Mr. A. Franklin ably

[44] For the experimental determination of the binding energy of the $He^3$ nucleus, see Li, Whaling, Fowler, and Lauritsen, Phys. Rev. **83**, 512 (1951).

[45] M. H. Mittelman, Phys. Rev. **107**, 1170 (1957).

[46] J. Traub and H. M. Foley (to be published).

assisted in taking data and performing calculations, and Mr. M. Reeber constructed most of the electronic equipment. One of us (E. D. C.) wishes to thank the Union Carbide and Carbon Corporation and the Radio Corporation of America for their generosity in awarding fellowships. Mrs. Frances Bennett provided expert stenographic aid in the preparation of the manuscript.

## APPENDIX I. ION SOURCE YIELD

We assume that the drawout potential removes all ions formed in region $V$ of Fig. 4. If $N$ is the number of ions removed per second, then

$$N=j^-\sigma^+nV/e,$$

where $j^-$ is the electron current density, $\sigma^+$ is the ionization cross section, $n$ is the gas density, and $e$ is the electronic charge. The ion current is then

$$\begin{aligned}I^+&=Ne=I^-\sigma^+nd\\&=I^-d\sigma^+p/kZ,\end{aligned}$$

where $I^-=j^-tL$, $p$ is the pressure in the bombardment region, and $d$, $t$, and $L$ are given in Fig. 4. For $p=10^{-4}$ mm Hg, $T=300°$K, and the present geometry, we have

$$I^+=1.4\times10^{-5}I^-$$

Experimentally $I^+=5\times10^{-5}I^-$ for this presssure. The low value of the estimate indicates that ions are actually drawn from a larger volume of the bombardment region than $V$.

## APPENDIX II. SPACE-CHARGE LIMITING OF THE ION CURRENT

The maximum ion current $I_i(\max)$ is given by[47]

$$I_i(\max)=\frac{\sqrt{2}}{\pi}\left(\frac{e}{m}\right)^{\frac{1}{2}}\frac{wD}{L^2}V^{\frac{3}{2}}\text{ esu/sec}=6\times10^{-8}\text{ amp},$$

where $V=(20/300)$ esu, $L=35$ cm, $w=3.0$ cm$=$beam width, $D=1.0$ cm$=$beam height. The Child's law relation is $I=AV^{\frac{3}{2}}/L^2$, where $A=$constant. If the ion current is given by this relation, we have

$$I_i=\text{const}\times v^3/L^2=\text{const}\times L/T^3,$$

where $T=$time of beam transit, and $v=$beam velocity. For a given line width $T$ is constant and $I_i=\text{const}\times L$. Thus, for a given line width, the space-charge limited ion current increases with $L$.

## APPENDIX III. THERMAL SPREADING OF THE ION BEAM

In the following estimate we neglect the complications which ensue when thermal spreading and space-charge effects are considered together. Let $L$ be the beam path length as before, and let $h$ be the width of the final aperture. Assume the beam issues from a line source with no spread in the longitudinal velocity component $v_z$. The transverse component $v_y$ is limited by the condition $v_y\leq Dv_z/2L$, where $v_z=(2eV/m)^{\frac{1}{2}}$. If we assume that the transverse velocities are given by a Maxwellian distribution, the fraction of particles for which the transverse component is less than the upper limit is given by

$$\eta=\frac{2}{\sqrt{\pi}}\int_0^{(m/2kT)^{\frac{1}{2}}v_y(\max)}\exp(-x^2)dx.$$

For $T=300°$K, $V=20$ ev, and the present geometry we find $\eta=0.6$. Thus approximately half of the ions might be lost to the beam through thermal spreading.

[47] J. R. Pierce, *Theory and Design of Electron Beams* (D. Van Nostrand and Company, Princeton, New Jersey, 1949).

## APPENDIX IV. RADIO-FREQUENCY STARK EFFECT

The rf electric field associated with the oscillating magnetic field in the hfs transition region couples the various hfs components of the $2\,^2S_{\frac{1}{2}}$ and $2\,^2P_{\frac{1}{2}}$ states. This produces a shift in the apparent value of the hfs splitting and a quenching of the metastable ions. An exact evaluation of these effects is prohibitively difficult. We show here that the formulas for the static Stark effect provide a good estimate in the high-frequency case if the amplitude of the static field is replaced by the rms value of the electric field. We consider a simplified problem in which the hfs is ignored and there exists instead a simple Zeeman resonance between magnetic sublevels of the $2\,^2S_{\frac{1}{2}}$ state. In addition it is assumed that there is an oscillating magnetic field, an oscillating electric field, and that the Zeeman splitting of the $2\,^2S_{\frac{1}{2}}$ state and the frequency of the fields are about 1083 Mc/sec. Thus the matrix elements and energy separations in the simplified problem are essentially the same as in the actual experiment. The energy levels are shown in Fig. 20.

In the presence of oscillating magnetic and electric fields the amplitude coefficients of the levels defined in Fig. 20 are governed by the equations:

$$\begin{aligned}\dot{a}&=-i\omega_a a+Me^{-i\omega t}b+2\mathcal{E}(\cos\omega t)d,\\\dot{b}&=-i\omega_b b-Me^{i\omega t}a-2\mathcal{E}(\cos\omega t)c,\\\dot{c}&=-i\omega_c c+2\mathcal{E}(\cos\omega t)b,\\\dot{d}&=-i\omega_d d-2\mathcal{E}(\cos\omega t)a.\end{aligned}$$

Here, $\omega$ is the frequency of the applied field in radians per second and

$$\begin{aligned}&\omega_a=E_a/\hbar,\quad \omega_c=E_c/\hbar-i\gamma/2,\quad M=\mu_0H_{1/2\hbar},\\&\omega_b=E_b/\hbar,\quad \omega_d=E_d/\hbar-i\gamma/2,\quad \mathcal{E}=(\tfrac{3}{4})^{\frac{1}{2}}ea_0E_{1/2\hbar},\end{aligned}$$

where $E_a$, $E_b$, $E_c$, and $E_d$ are the energies of the various states, $\gamma$ is the decay constant of the $2\,^2P_{\frac{1}{2}}$ state, and $H_1$ and $E_1$ are the peak amplitudes of the oscillating electric and magnetic fields, respectively. It is assumed that these fields are perpendicular to each other and

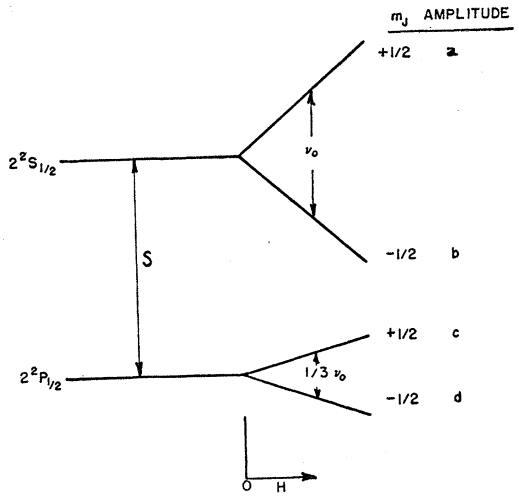


FIG. 20. Zeeman splitting of the $2\,^2S_{\frac{1}{2}}$ and $2\,^2P_{\frac{1}{2}}$ states in the absence of hyperfine structure. The letters $a$, $b$, $c$, and $d$ denote both the states and their probability amplitudes and $S$ is the Lamb shift. The Zeeman splitting $\nu_0$ is assumed to be about 1083 Mc/sec.

to the static magnetic field. The imaginary parts of $\omega_c$ and $\omega_d$ are introduced to account for the decay of the $2\,^2P_{\frac{1}{2}}$ state. We have dropped the antiresonant terms in the magnetic perturbation since the effect of these is known to be small. It can be readily shown that the damping of the $2P$ state has little effect on the static Stark shift. For simplicity we will also neglect it here; this is allowable as long as the frequency of the rf electric field is far removed from the Lamb shift frequency. Using methods developed by Ramsey[48] and Winter,[49] it can be shown that the frequency of the Zeeman transition in the presence of the rf electric field is given by

$$\omega=\omega_0-\left[\frac{\mathcal{E}^2}{\omega_b-\omega_c-\omega}+\frac{\mathcal{E}^2}{\omega_b-\omega_c+\omega}\right]+\left[\frac{\mathcal{E}^2}{\omega_a-\omega_d-\omega}+\frac{\mathcal{E}^2}{\omega_a-\omega_d+\omega}\right],$$

where $\omega_0=2\pi\nu_0$. Since $\omega$ is small compared to $(\omega_b-\omega_c)$ and $(\omega_a-\omega_d)$, this expression may be expanded in powers of $\omega$. In such an expansion the linear terms in $\omega$ cancel and we have

$$\omega=\omega_0-\frac{3}{4}a_0^2\frac{e^2}{\hbar^2}\frac{E_1^2}{2}\left[\frac{1}{\omega_b-\omega_c}-\frac{1}{\omega_a-\omega_d}\right].$$

The terms that we have neglected here amount to no more than one percent of the net shift. This result is identical to that obtained for a static field of magnitude $E_1/\sqrt{2}$ and we have shown that the formulas for the static Stark shift provide a good estimate of the rf Stark shift provided we take $E=E_1/\sqrt{2}$. A similar conclusion holds for the rf Stark quenching.

[48] N. F. Ramsey, Phys. Rev. **100**, 1191 (1955).
[49] J. Winter *et al.*, Compt. rend. **241**, 556 (1955).